Monthly Notices
of the
ROYAL ASTRONOMICAL SOCIETY

MNRAS **466,** 496–519 (2017)
Advance Access publication 2016 November 30

doi:10.1093/mnras/stw3091

X-ray-emitting active galactic nuclei from $z = 0.6$ to 1.3 in the intermediate- and high-density environments of the ORELSE survey

N. Rumbaugh,[1⋆] B. C. Lemaux,[2] A. Tomczak,[2] D. D. Kocevski,[3] L. M. Lubin,[2] P.-F. Wu,[4] R. R. Gal,[5] L. Shen,[2] A. Mansheim,[2] C. D. Fassnacht[2] and G. K. Squires[6]

[1]*National Center for Supercomputing Applications, University of Illinois, 1205 West Clark St., Urbana, IL 61801, USA*
[2]*Department of Physics, University of California, Davis, 1 Shields Avenue, Davis CA 95616, USA*
[3]*Department of Physics and Astronomy, Colby College, Waterville, ME 04901, USA*
[4]*Max-Planck Institut für Astronomie, Königstuhl 17, D-69117 Heidelberg, Germany*
[5]*University of Hawai'i, Institute for Astronomy, 2680 Woodlawn Drive, HI 96822, USA*
[6]*Spitzer Science Center, California Institute of Technology, M/S 220-6, 1200 E. California Blvd., Pasadena, CA, 91125, USA*

Accepted 2016 November 25. Received 2016 November 19; in original form 2016 July 28

ABSTRACT

We studied active galactic nucleus (AGN) activity in 12 large-scale structures (LSSs) in the Observations of Redshift Evolution in Large-Scale Environments (ORELSE) survey, at $0.65 < z < 1.28$, using a combination of *Chandra* observations, optical and NIR imaging and spectroscopy. We located a total of 61 AGNs that were successfully matched to optical counterparts in the LSSs. We found that AGN populations across our sample had more recently had starburst events compared to the overall galaxy populations. We find no relation between AGN activity and location within the LSSs, suggesting triggering mechanisms that depend on global environment are at most sub-dominant. To focus on differences between our AGNs, we grouped them into four sub-samples based on the spectral properties of their parents LSSs. We found one of the sub-samples, SG0023 & SC1604, stood out from the others. AGNs in this sample were disproportionately luminous. These AGNs had the most recent starburst events, in contrast to their parent populations. Additionally, both the AGNs and the overall galaxy population in SG0023 & SC1604 had the largest fraction of close kinematic pairs, which indicates a higher rate of galaxy mergers and interactions. These results suggest that major mergers are driving AGN activity in SG0023 & SC1604, while other processes are likely triggering less luminous AGNs in the rest of our sample. Additionally, minor mergers are unlikely to play a significant role, since the same conditions that lead to more major mergers should also lead to more minor mergers, which is not observed in SG0023 & SC1604.

Key words: galaxies: active – galaxies: clusters: general – galaxies: evolution – galaxies: nuclei – X-rays: galaxies.

1 INTRODUCTION

The current consensus is that all massive galaxies contain a supermassive black hole (SMBH; e.g. Kormendy & Richstone 1995; Ford et al. 1998; Graham 2016). While the presence of SMBHs can be inferred through their gravitational influences, they can also be directly observed as they accrete material, fuelling emission across a wide spectrum. While most SMBHs have low luminosities that preclude observation, a small subset, active galactic nuclei (AGNs), are some of the most powerful emitters in the Universe. Numerous studies have found connections between the evolution of the central SMBH and that of its host galaxy. In the local Universe the masses of SMBHs and the masses and velocity dispersions of their hosts' central bulges or spheroids have been shown to be correlated (Ferrarese & Merritt 2000; Tremaine et al. 2002; Marconi & Hunt 2003; Häring & Rix 2004; Xu et al. 2007; Graham 2016). As redshift increases up to $z \sim 2$, so do both star formation rates and AGN fractions (Boyle & Terlevich 1998; Silverman et al. 2008; Bluck et al. 2011). Across a wide redshift range, AGNs have been observed to be associated with star-forming galaxies (e.g. Kauffmann et al. 2003; Heckman et al. 2004; Veilleux et al. 2009; Laird et al. 2010; Georgantopoulos, Rovilos & Comastri 2011; Juneau et al. 2013; Lemaux et al. 2014).

While the evidence for a connection between SMBH and galaxy evolution is strong, consensus has not yet been reached on the processes that fuel SMBH growth and AGN activity. A number of mechanisms that can trigger AGN activity have been proposed. One such mechanism is major galaxy mergers, which can create inflows of gas to galactic nuclei, fuelling bulge growth and an AGN

⋆ E-mail: rumbaugh@illinois.edu

Table 1. Properties of observed ORELSE LSSs.

LSS	RA[a] (J2000)	Dec.[a] (J2000)	$\langle z \rangle$	z lower bound	z upper bound	Num. of known clusters	Num. of known groups	σ range[b]	Confirmed members[c]	Confirmed AGN[c]
SG0023	00 23 51	+04 22 55	0.84	0.82	0.87	0	5	200–500	244	7
RCS0224	02 24 36	−01 55 58	0.77	0.76	0.79	2	1	200–800	119	4
Cl0849	08 48 47	+44 54 06	1.26	1.25	1.28	2	0	[d]	74	4
RXJ0910	09 10 40	+54 19 57	1.11	1.08	1.15	2	0	500–900	142	9
RXJ1053	10 53 40.2	+57 35 22.3	1.14	1.10	1.15	1 to 2	0	880 ± 130	72	1
RXJ1221	12 21 26.1	+49 18 30.7	0.70	0.69	0.71	1	1	800–850	160	4
SC1324	13 24 45	+30 34 18	0.76	0.65	0.79	3	1	150–1000	454	8
Cl1350	13 50 48.3	+60 07 11.5	0.80	0.79	0.81	1	2	200–1000	102	3
SC1604	16 04 15	+43 16 24	0.90	0.84	0.96	5	3	150–1100	531	10
RXJ1716	17 16 54	+67 08 47	0.81	0.80	0.83	2	0	750–1150	144	4
RXJ1757	17 57 19.0	+66 31 27.8	0.69	0.68	0.71	1	0	540 ± 140	75	2
RXJ1821	18 21 32.3	+68 27 55.4	0.82	0.80	0.84	1	0	1150 ± 120	131	5

[a]Coordinates for LSSs with more than one cluster are the approximate central positions, while the others are given as the centroid of the peak of diffuse X-ray emission associated with the respective cluster.
[b]In units of km s^{-1}. For LSSs with more than group or cluster, this measurement is the range of velocity dispersions of groups and clusters within the LSS. All velocity dispersions are measured within 1 Mpc.
[c]Spectroscopically confirmed objects ($Q = 3,4$) within the redshift bounds of the LSS; see Section 3.1 for quality flag details.
[d]Velocity dispersion not measured.

(Hopkins et al. 2006; Narayanan et al. 2008). Many others have been proposed, as well, including minor mergers or tidal interactions (Moore et al. 1996; Menanteau, Jimenez & Matteucci 2001; Younger et al. 2008; Georgakakis et al. 2009), processes such as disc or bar instabilities or turbulence (Elmegreen et al. 1998; Genzel et al. 2008; Younger et al. 2008; Hopkins & Quataert 2010; Bournaud et al. 2011) and recycling of stellar material (Ciotti & Ostriker 2007).

There is growing evidence that not one mechanism is responsible for creating all AGNs. While major galaxy mergers are thought to fuel some of the brightest AGNs, they are not common and are likely not responsible for all AGNs (see, e.g. Wild et al. 2007; Reichard et al. 2009; Kormendy & Ho 2013; Heckman & Best 2014). Some evidence has been found of an association between merging galaxies or those with signs of recent mergers or interactions (Kocevski et al. 2009; Koss et al. 2010; Treister et al. 2012; Ellison et al. 2013; Hernández-Ibarra et al. 2016), but it is likely this is representative of only a subset of the AGN population, since large numbers of AGNs have been found associated with hosts not likely to have recently undergone major mergers (Georgakakis et al. 2009; Cisternas et al. 2011; Schawinski et al. 2011; Kocevski et al. 2012; Rosario et al. 2012; Koulouridis et al. 2014). While major mergers are thought to be important at the high-luminosity end, there is a dearth of evidence supporting alternative mechanisms for triggering lower luminosity AGNs and a multitude of options (Schawinski et al. 2012; Netzer 2015).

The question, now, is what exactly are the dominant AGN triggering mechanisms and what conditions lead to their activation? Optimally, AGNs should be examined across a wide range of redshifts and environments. We have assembled such a sample as part of the Observations of Redshift Evolution in Large-Scale Environments (ORELSE; Lubin et al. 2009) survey. The ORELSE survey is a systematic search for large-scale structures (LSSs) around an original sample of 20 galaxy clusters in a redshift range of $0.6 < z < 1.3$, designed to study galaxy properties over a wide range of local and global environments. The survey has revealed superclusters (i.e. LSSs with three or more member clusters) and merging systems, and has also found some of the initially targeted galaxy clusters to be isolated systems. This provides an excellent laboratory for studying AGN activity. The wide range of environments means the sample likely contains infalling populations where major mergers between blue galaxies are more prevalent, and one system, the Cl1604 supercluster, has already been shown to have AGNs associated with mergers (Kocevski et al. 2009). Additionally, both star formation and AGN activity are known to increase with redshift (Boyle & Terlevich 1998; Silverman et al. 2008; Bluck et al. 2011), so the higher redshift of our sample and the wide range provide an ideal set for examining AGN activity and how it relates to galaxy evolution.

12 of the systems in the ORELSE survey have *Chandra* imaging with which we can study AGNs at the redshifts of the LSSs. We have extensive optical imaging and spectroscopy across the sample to complement the X-ray data set. In this paper, we use the *Chandra* imaging of these 12 systems to locate AGNs within them and measure their X-ray luminosities. We couple this with the optical properties of their hosts and the underlying galaxy populations to investigate AGN triggering mechanisms and their relation to galaxy evolution. For our cosmological model, we assume $\Omega_m = 0.3$, $\Omega_\Lambda = 0.7$ and $h = H_0/70\,\mathrm{kms^{-1}Mpc^{-1}}$.

We first discuss the LSSs in our sample in Section 2. We describe our observations, data reduction and methods for locating AGNs in Section 3. In Section 4, we examine the properties of the global galaxy populations in our sample and divide our sample into several sub-samples based on their properties. We then analyse the AGN populations in Section 5, followed by a discussion in Section 6.

2 THE ORELSE LSS SAMPLE

In this section, we describe our sample that is more succinctly summarized in Table 1. As described in Section 1, our sample consists of all LSSs in the ORELSE survey with useful *Chandra* imaging. This consists of 12 systems,[1] composed of both observations taken

[1] A 13th system, Cl1137+3000, also has *Chandra* imaging, but the shallow exposure (less than half the next shortest exposure time in our sample) and the high redshift of the cluster mean that it is not useful for our analysis.

specifically for the ORELSE survey and other publicly available archived data.

The redshift boundaries defined below were determined by visually examining the redshift distribution of each LSS's galaxy population. Delineating where LSSs end is not straightforward, complicated by associated filaments or possible nearby sheets. The redshift boundaries are chosen conservatively, in the sense of including all galaxies that could be part of each overall LSS.

The details of some of the LSSs in our sample, Cl0023 supergroup, the RXJ0910 LSS, the Cl1324 supercluster, the Cl1604 supercluster and the clusters RXJ1757.3+6631 and RXJ1821.6+6827 (hereafter SG0023, RXJ0910, SC1324, SC1604, RXJ1757 and RXJ1821, respectively) have been discussed in previous works. For more information on these LSSs, see Rumbaugh et al. (2012), Rumbaugh et al. (2013), Mansheim et al. (in preparation) and the references therein. The remaining LSSs in our sample are described below.

2.1 RCS J0224-0002.5

The optically selected $z = 0.77$ galaxy cluster RCS J0224-0002.5 (hereafter RCS0224) was discovered by Gladders, Yee & Ellingson (2002) as part of the Red-Sequence Cluster Survey (RCS; Gladders & Yee 2005). They found two to four lensed background objects and fit a lensing model consistent with a velocity dispersion of $\sim$1000 km s^{-1} for the cluster. Hicks et al. (2007) used 101 ks of *Chandra* observations to measure an integrated cluster temperature of $5.1^{+0.9}_{-0.5}$ keV. Using the same data, Hicks et al. (2008) measured an X-ray luminosity within R_{500} of $4.4 \pm 0.5 \times 10^{44}$ erg s^{-1}. They investigated scaling relations between several cluster parameters, including L_X, T_X, $M_{\rm tot}$ and Y_X, and found the cluster to be in general agreement.

2.2 Cl0849

The Cl0849 LSS contains at least two clusters within close proximity and at known similar redshifts of $z \sim 1.26$. The infrared (IR)-selected galaxy cluster RXJ0848.6+4453 at $z = 1.26$ was discovered as part of a deep field survey (Stanford et al. 1997). A soft-band (0.5–2.0 keV) X-ray luminosity was measured of $0.8 \pm 0.3 \times 10^{44}$ erg s^{-1} using archival *ROSAT* data (Rosati et al. 1999). Only 4.2 arcmin away, RXJ0848.9+4452 was discovered as part of the *ROSAT* Deep Cluster Survey (Rosati et al. 1999). They measured a soft-band X-ray luminosity of $1.5 \pm 0.3 \times 10^{44}$ erg s^{-1}. *Chandra* imaging of RXJ0848.9+4452 yielded an X-ray temperature of $5.8^{+2.8}_{-1.7}$ keV and a bolometric X-ray luminosity of $3.3^{+0.9}_{-0.5} \times 10^{44}$ erg s^{-1} (Stanford et al. 2001), in approximate agreement with scaling relations.

2.3 RXJ1053+5735

RXJ1053+5735 (hereafter RXJ1053), an X-ray-selected cluster at $z = 1.14$, was discovered in *ROSAT* ultra-deep HRI imaging of the Lockman Hole (Hasinger et al. 1998). They observed an unusual double-lobed profile in the extended X-ray emission. Using *XMM–Newton*, Hashimoto et al. (2002) measured an X-ray temperature of $4.9^{+1.5}_{-0.9}$ keV and a bolometric X-ray luminosity of $3.4 \pm 0.34 \times 10^{44}$ erg s^{-1}. Both X-ray redshifts and redshifts of member galaxies are concordant between the lobes that are only $\sim$250 kpc apart, suggesting an equal-mass cluster merger (Hashimoto et al. 2005).

2.4 RXJ1221+4918

RXJ1221+4918 (hereafter RXJ1221) is an X-ray-selected cluster at $z = 0.70$. It was serendipitously detected in the 160 deg^2 *ROSAT* Position Sensitive Proportional Counter survey (Vikhlinin et al. 1998). Vikhlinin et al. (2002) measured an X-ray temperature of 7.2 ± 0.6 keV for the cluster and soft-band and bolometric X-ray luminosities of 7.0 and 28.7×10^{44} erg s^{-1}, respectively. There has been repeated analysis of the cluster, with Mullis et al. (2003) measuring a soft-band X-ray luminosity of 4.27×10^{44} erg s^{-1} for the cluster, while Ettori et al. (2004) measured an X-ray temperature of $7.5^{+0.7}_{-0.6}$ keV and a bolometric X-ray luminosity of $12.95 \pm 0.39 \times 10^{44}$ erg s^{-1}, and Vikhlinin et al. (2009) measured a temperature and soft-band luminosity of 6.63 ± 0.75 keV and 3.35×10^{44} erg s^{-1}, respectively.

2.5 Cl1350.0+6007

Cl1350.0+6007 (hereafter Cl1350) is an X-ray-selected cluster at $z = 0.80$, discovered in the *ROSAT* Deep Cluster Survey (Rosati et al. 1998). Using *Chandra* data, Holden et al. (2002) measured an X-ray temperature of $4.9^{+0.7}_{-0.6}$ keV and a bolometric X-ray luminosity of $4.1^{+0.5}_{-0.4} \times 10^{44}$ erg s^{-1}. Also with *Chandra*, Jeltema et al. (2005) measured an X-ray luminosity of 2.3×10^{44} erg s^{-1} in the 0.3–7.0 keV range.

2.6 RXJ1716.9+6708

RXJ1716.9+6708 (hereafter RXJ1716) is an X-ray-selected cluster at $z = 0.81$. Henry et al. (1997) discovered the cluster in the *ROSAT* All-Sky Survey (Voges et al. 1996) of the north ecliptic pole and measured a soft-band X-ray luminosity of $3.2 \pm 0.9 \times 10^{44}$ erg s^{-1}. Follow-up observations using the *ROSAT* High-Resolution Imager yielded an X-ray temperature of $5.66^{+1.37}_{-0.58}$ keV and a hard 2–10 keV X-ray luminosity of $8.19 \pm 0.43 \times 10^{44}$ erg s^{-1} in the 0.3–7.0 keV range. Using *Chandra* data, Jeltema et al. (2005) measured an X-ray luminosity of 5.6×10^{44} erg s^{-1} in the 0.3–7.0 keV range. See Lemaux et al. (in preparation) for more details on this LSS.

3 OBSERVATIONS AND REDUCTION

3.1 Optical and NIR observations

In analysing the AGN hosts, we use ground-based imaging data obtained for each field with either the Large Format Camera (LFC; Simcoe et al. 2000) on the Palomar 5 m telescope or the Suprime-Cam (Miyazaki et al. 2002) on the *Subaru* 8-m telescope. The LFC observations were taken using Sloan Digital Sky Survey (SDSS)-like r', i' and z' filters. We hereafter refer to these LFC filters, or the equivalents from the Suprime-Cam data, as *R*, *I* and *Z*. Additionally, photometric redshift catalogues have been created for a subset of our sample, which we use to examine the effects of completeness on our analysis and to calibrate our 'supercolour' parametrization described in Section 4.1. For these catalogues, we use the LFC and *Subaru* data (in total, *B*-, *V*-, *Rc*, *R*+, *Ic*-, *I*+, *Z*+ and *Y*-band data were taken using Suprime-Cam), as well as *J*- and *K*-band data taken using the United Kingdom Infrared Telescope Wide Field Camera (Hewett et al. 2006), *J*- and *Ks*-band data using the Wide-field InfraRed Camera (Puget et al. 2004) on the Canada–France–Hawai'i Telescope, and 3.6, 4.5, 5.8 and 8.0 μ data using the Infrared Array Camera (IRAC; Fazio et al. 2004) on the *Spitzer* telescope. Which telescope data are available varies by LSS. For more descriptions of

Table 2. DEIMOS spectroscopic observation characteristics.

LSS	Central λ (Å)	Approx. spectral coverage (Å)	Exp. time range (s)	Avg. seeing range (arcsec)
SG0023	7500–7850	6200–9150	5700–9407	0.45–0.81
RCS0224	7300–7450	6000–8750	6840–7520	0.53–0.88
Cl0849	8700	7400–10 000	6300–16 200	0.51–1.5
RXJ0910	8000–8100	6700–9400	7200–11 664	0.5–1.05
RXJ1053	8200	6900–9500	7200–9000	0.56–0.79
RXJ1221	7200	5900–8500	4860–8400	0.55–1.2
SC1324	7200	5900–8500	2700–10 800	0.44–1.0
Cl1350	7500	6200–8800	3600–10 400	0.5–1.55
SC1604	7700	6385–9015	3600–14 400	0.5–1.3
RXJ1716	7800	6500–9100	5400–9000	0.54–0.83
RXJ1757	7000–7100	5700–8400	6300–14 730	0.47–0.82
RXJ1821	7500–7800	6200–9100	7200–9000	0.58–0.86

the reductions, see Gal et al. (2008), Lemaux et al. (in preparation) and Tomczak et al. (in preparation).

SC1604 was also imaged using the Advanced Camera for Surveys (ACS) on-board the *Hubble Space Telescope* (*HST*). The *HST* imaging for SC1604 consists of 17 ACS pointings designed to image 9 of the 10 galaxy density peaks in the field. Observations were taken using the *F606W* and *F814W* bands. These bands roughly correspond to broad-band *V* and *I*, respectively. See Kocevski et al. (2009) for details on the ACS reduction.

3.1.1 Photometric redshift catalogues

To extract photometric redshifts and other characteristics of our galaxy populations, we performed spectral energy distribution (SED) fitting on our imaging data. Results from aperture photometry were used to run the Easy and Accurate $z_{\rm phot}$ from Yale (EAZY; Brammer, van Dokkum & Coppi 2008) code that performs an iterative χ^2 fit using Projet d'Étude des GAlaxies par Synthèse Évolutive (PÉGASE; Fioc & Rocca-Volmerange 1997) models. This code outputs $P(z)$, a measure of our confidence that the respective source is at a given redshift. The redshift at which $P(z)$ peaks was adopted as the photometric redshift, $z_{\rm peak}$. A second round of fitting with purely stellar templates was carried out to locate the stars in our sample. We removed from our sample likely stars and objects with an S/N < 3 in the detection band, those covered in less than five of the broad-band images, with significant saturation, or with poor fits to galaxy SEDs.

A final stage of fitting was carried out using the Fitting and Assessment of Synthetic Templates (Kriek et al. 2009) code. High-quality spectroscopic redshifts were used when available and $z_{\rm peak}$ from EAZY was used as a redshift prior for all other cases. From the EAZY output, we derived rest-frame magnitudes for all our sources, except those excised as described above. This SED fitting has so far been carried out on SG0023, RXJ0910, SC1324, SC1604, RXJ1716, RXJ1757 and RXJ1821. See Lemaux et al. (in preparation) and Tomczak et al. (in preparation) for more details on the photometric catalogues and SED fitting.

3.1.2 Spectroscopy

Our photometric catalogue is complemented by extensive spectroscopic data. For this part of the study, we used the Deep Imaging Multi-Object Spectrograph (DEIMOS; Faber et al. 2003) on the Keck II 10 m telescope. In addition, SG0023, RXJ0910, SC1604 and RXJ1821 have some LRIS coverage (see Oke, Postman & Lubin 1998; Gal & Lubin 2004; Gioia et al. 2004; Tanaka et al. 2008). DEIMOS has a wide field of view (16.9 arcmin × 5.0 arcmin), high efficiency and is able to position over 120 targets per slit mask, which makes the instrument ideal for establishing an extensive spectroscopic catalogue. We targeted objects as faint as ∼25, with most objects having $m_{i'} \leq 24.5$. On DEIMOS, we used the 1200 line mm^{-1} grating, blazed at 7500 Å and 1 arcsec-wide slits. These specifications create a pixel scale of 0.33 Å pixel^{-1} and a full width at half-maximum resolution of ∼1.7 Å. The central wavelength was varied from LSS to LSS and sometimes between different masks for the same LSS. Our setup provided wavelength coverage approximately within 1300 Å of the central wavelengths. Central wavelengths for the spectroscopic observations for the 12 LSSs and the approximate spectral coverages are displayed in Table 2. When more than one central wavelength was used per LSS, a range is given. Total exposure times for the observations are in the range of 1–4.5 h per mask and varied based on conditions and *i*'-band distributions of targets.

Spectroscopic targets were chosen based on colour and magnitude, following the method of Lubin et al. (2009). The number of spectroscopic targets in each LSS is shown in Table 3. Redshifts were determined or measured for all targets and given a quality flag value, Q, where $Q = 1$ indicates that we could not determine a secure redshift, $Q = 2$ means a redshift was obtained using features that were only marginally detected, $Q = 3$ means one secure and one marginal feature were used to calculate the redshift and $Q = 4$ meant at least two secure features were used. Those sources determined to be stars were given a flag of -1. See Gal et al. (2008) and Newman et al. (2013) for more details on quality flags and the spectral targeting method. For our analysis, extragalactic redshifts with $Q = 3,4$ were deemed satisfactory and the number of such sources in field of each LSS is shown in Table 3. We measured an average of ∼800 high-quality redshifts per LSS, with the number of $Q = 3,4$ redshifts in the field of view for each LSS ranging from 410 for RXJ1053 to 1849 for SC1604.

3.2 X-ray observations

All X-ray imaging of the clusters was conducted with the Advanced CCD Imaging Spectrometer (ACIS) of the *Chandra* X-ray Observatory. The instrument has 10 CCDs; four are arranged in a square with a 16.9 arcmin × 16.9 arcmin field of view, while the others are arranged in a line parallel to the bottom of this square, with a field of view of 8.3 arcmin × 50.6 arcmin. The ACIS-I array has an aimpoint

Table 3. Spectroscopic and X-ray catalogue information.

LSS	Spectroscopic targets	Spectroscopic redshifts[a]	X-ray sources, $>3\sigma$ ($>2\sigma$)[b]	X-ray sources, matched[c]	Attempted redshifts[d]	Confirmed redshifts[e]
SG0023	1155	943	92(109)	66(80)	43(51)	29(35)
RCS0224	619	507	119(138)	92(106)	7(8)	7(8)
Cl0849	926	522	183(214)	120(143)	26(31)	13(17)
RXJ0910	991	750	218(248)	125(141)	43(46)	27(30)
RXJ1053	704	410	115(131)	82(94)	22(25)	7(8)
RXJ1221	681	535	133(156)	81(96)	33(36)	19(22)
SC1324	1690	1352	179(215)	122(140)	49(60)	33(41)
Cl1350	828	638	85(101)	53(66)	23(27)	17(21)
SC1604	2445	1849	144(179)	101(125)	44(50)	27(30)
RXJ1716	828	571	95(118)	80(94)	23(29)	10(11)
RXJ1757	970	757	84(98)	59(65)	38(40)	22(24)
RXJ1821	744	626	95(110)	63(72)	44(49)	24(29)

[a]Includes all redshifts obtained, regardless of whether they were within the redshift bounds of the LSS. Only includes highquality redshifts.
[b]Includes sources with a significance $>3\sigma$ ($>2\sigma$) in at least one of the three bands: soft, hard or full.
[c]X-ray sources matched to optical counterparts.
[d]Includes all X-ray sources that were targeted for spectroscopy, regardless of the quality of measured redshift.
[e]Only includes highquality redshifts for objects matched to X-ray point sources.

Table 4. *Chandra* observations.

Observation ID	Target	Instrument	PI	Exposure time (ks)	RA[a]	Dec.[a]
7914	SG0023	ACIS-I	Lubin	49.38	00 23 52.30	04 22 34.20
3181	RCS0224	ACIS-S	Gladders	14.37	02 24 34.10	−00 02 30.90
4987	RCS0224	ACIS-S	Ellingson	88.97	02 24 34.10	−00 02 30.90
927	Cl0849	ACIS-I	Stanford	125.15	08 48 55.90	44 54 50.00
1708	Cl0849	ACIS-I	Stanford	61.47	08 48 55.90	44 54 50.00
2227	RXJ0910	ACIS-I	Stanford	105.74	09 10 45.41	54 22 05.00
2452	RXJ0910	ACIS-I	Stanford	65.31	09 10 45.41	54 22 05.00
4936	RXJ1053	ACIS-S	Predehl	92.4	10 53 43.00	57 35 00.00
1662	RXJ1221	ACIS-I	van Speybroeck	79.08	12 21 24.50	49 18 14.40
9403	SC1324	ACIS-I	Lubin	26.94	13 24 49.50	30 51 34.10
9404	SC1324	ACIS-I	Lubin	30.4	13 24 42.50	30 16 30.00
9836	SC1324	ACIS-I	Lubin	20	13 24 42.50	30 16 30.00
9840	SC1324	ACIS-I	Lubin	21.45	13 24 49.50	30 51 34.10
2229	Cl1350	ACIS-I	Stanford	58.31	13 50 46.10	60 07 09.00
6932	SC1604	ACIS-I	Lubin	49.48	16 04 19.50	43 10 31.00
6933	SC1604	ACIS-I	Lubin	26.69	16 04 12.00	43 22 35.40
7343	SC1604	ACIS-I	Lubin	19.41	16 04 12.00	43 22 35.40
548	RXJ1716	ACIS-I	van Speybroeck	51.73	17 16 52.30	67 08 31.20
10443	RXJ1757	ACIS-I	Lubin	21.75	17 57 19.80	66 31 39.00
11999	RXJ1757	ACIS-I	Lubin	24.7	17 57 19.80	66 31 39.00
10444	RXJ1821	ACIS-I	Lubin	22.24	18 21 38.10	68 27 52.00
10924	RXJ1821	ACIS-I	Lubin	27.31	18 21 38.10	68 27 52.00

[a]Coordinates refer to those of the observation aimpoint.

on the I3 chip, near the centre of the square area, while the aimpoint of the ACIS-S array is on the S3 chip, near the centre in the line array. While most (19) of the observations used for this study employ the ACIS-I array, three observations taken from the archive used the ACIS-S array instead. In either case, the five to six CCDs closest to the aimpoint are typically used for each observation. SC1604 and SC1324, with angular sizes in excess of 20 arcmin, were observed with two pointings each of the ACIS-I array. For SC1604, the two pointings are meant to cover as much of the LSS as possible and there is only a small overlap between the two pointings ($\sim$30 arcmin^2). For SC1324, the two pointings are centred near the two largest and originally discovered clusters, SC1324+3011 and SC1324+3059. There is an approximately 13 arcmin gap between the north and south pointings. All other LSSs were observed with one pointing. Total exposure times ranged from 45 to 190 ks. Details of the observations are summarized in Table 4.

3.3 X-ray data reduction and photometry

The reduction of the data was conducted using the *Chandra* Interactive Analysis of Observations 4.7 software (CIAO; Fruscione et al. 2006). We used the Imperial reduction pipeline that is described in detail in Laird et al. (2009) and Nandra et al. (2015). We will briefly summarize it here.

For each individual observation, we corrected for aspect offsets, applied a destreaking algorithm, removed bad pixels and cosmic

rays, corrected for charge-transfer inefficiency and gain effects and applied the ACIS particle background cleaning algorithm. Unlike in Nandra et al. (2015), data for all available ACIS chips were reduced, instead of restricting the reduction to just ACIS Chips 0–3. This was necessary, as some observations had aimpoints on other ACIS chips. For each observation, flaring events were detected and excised. After all of these corrections, the astrometry was corrected using our spectroscopic catalogues for reference.

Event files were then created in four different energy bands: soft (0.5–2.0 keV), hard (2.0–7.0 keV), ultrahard (4.0–7.0 keV) and full (0.5–7.0 keV). Exposure maps were created for each band using the task *merge_obs*, with spectral weights corresponding to a power law with $\Gamma = 1.4$, where Γ refers to the slope. For LSSs with more than one observation, the individual images and exposure maps were then stacked.

Point source detection was carried out in a two-step, iterative process. First, the task *wavdetect* was run for each image (in each band) at a probability threshold of 10^{-4}, designed to detect virtually all real sources, but also introducing many spurious detections. Aperture photometry was then carried out on all detections in the following manner. Source counts were measured in a circular aperture centred on the detection position with a radius such that 70 per cent of the source's flux should be enclosed.[2] The background was measured in an annulus with an inner radius equal to 1.5 times that of a circle containing 95 per cent of the source flux and an outer radius 100 pixels larger. Other detected point sources were excluded when measuring background counts, which means that spurious detections could cause underestimation of the background at this step. To compensate, the probability of false detections was then calculated using Poisson statistics. Sources above the probability threshold of 4×10^{-6} were cut and the aperture photometry was then recalculated with a more accurate background estimation with fewer false sources improperly masked.

All detected sources that made it through the probability cut, in all bands, were merged into a single catalogue and each detection was checked by eye. For our final aperture photometry, we measured soft band fluxes using the 95 per cent enclosed energy radii, while we used the 90 per cent enclosed energy radii for the hard and full bands. The smaller enclosed energy radii for the hard and full bands were chosen because of the excessively large size of the 95 per cent enclosed energy radii in these bands. Fluxes were estimated using the Bayesian method described in Laird et al. (2009), using a power-law spectral model with $\Gamma = 1.4$. The aperture photometry was also used to estimate detection significances according to the formula

$$\sigma = C / \left(1 + \sqrt{0.75 + B}\right), \quad (1)$$

where C and B are the net source counts and background counts within the aperture, respectively (Gehrels 1986).

3.4 Optical matching

To search for AGNs within the individual clusters, we matched our X-ray point sources to optical catalogues. Only objects with detection significances, in at least one band, above 2σ were considered.[3] We used the maximum likelihood ratio technique described in Rumbaugh et al. (2012), which was developed by Sutherland & Saunders (1992) and also used by Taylor et al. (2005), Gilmour et al. (2007) and Kocevski et al. (2009). The main statistic calculated in each case is the likelihood ratio (LR), which estimates the probability that a given optical source is the genuine match to a given X-ray point source relative to the arrangement of the two sources arising by chance. The LR is given by the equation

$$LR_{i,j} = \frac{w_i \exp\left(-r_{i,j}^2 / 2\sigma_j^2\right)}{\sigma_j^2}. \quad (2)$$

Here $r_{i,j}$ is the separation between objects i and j, σ_j is the positional error[4] of object j and $w_i^2 = 1/n\,(<m_{\rm I})$ is the inverse of the number density of optical sources with magnitude fainter than $m_{\rm I}$. The inclusion of the latter quantity is designed to weight against matching to fainter optical objects that are more likely to have chance projections. For each X-ray source, we carried out a Monte Carlo (MC) simulation to estimate the probability that each optical counterpart is the true match using the LRs. In the case of a single match, we threw out those with a probability of being spurious >15 per cent. See Rumbaugh et al. (2012) for more details on the method. The number of X-ray sources matched to optical counterparts is given in Table 3.

For each LSS, except SC1604, $n(<m_{\rm I})$ was measured using I magnitudes from our LFC/Suprime-Cam catalogues. For SC1604, ACS data were also available, but these observations did not cover the entire LSS. All objects were matched to the LFC/Suprime-Cam catalogues. When possible, objects were also matched using the *F814W* magnitude from the ACS catalogues and matches to ACS objects took precedence.

4 GLOBAL LSS PROPERTIES

The 12 LSSs in our sample span a wide range of redshifts, sizes and evolutionary states. There are a number of isolated clusters, such as RXJ1757 and RXJ1821, several LSSs in the process of merging, such as the supergroup SG0023 and the merging clusters of RXJ1053, as well as several superclusters, including SC1324 and SC1604. We would like to investigate the differences between the AGNs across this wide range of environments, through which we can learn about their triggering mechanisms and the effects the environments have on active galaxies. To accomplish this, we first study the global properties of the LSSs in our sample.

4.1 The red sequence and the blue populations

A colour–magnitude diagram (CMD) provides information on the evolutionary states of a LSS's galaxy population. When the colours of galaxies at a common redshift are plotted against their magnitudes on a CMD, they generally separate out into two regions: the red sequence that largely contains older, quiescent galaxies, and the blue cloud that is characterized by younger, actively star-forming populations. Intermediate to these is the green valley that is usually sparsely populated and may be a transitional region where blue galaxies are rapidly evolving on to the red sequence after star

[2] The *Chandra* point spread function (PSF) was calculated using the MARX simulator (Wise et al. 2003). See Laird et al. (2009).

[3] We used 2σ as our threshold instead of 3σ because being successfully matched to an optical source increases the confidence in the detection of an X-ray object.

[4] Positional errors of X-ray sources were calculated using the method of Kim et al. (2007). Optical positional errors are assumed to be negligible in comparison. Note also that 1.5 arcmin was used as the minimum X-ray positional error.

formation ceases (Faber et al. 2007) or rejuvenated red sequence galaxies (Dressler et al. 2013).

Because of the redshift range of our sample, using the same bands for magnitudes and colours across all LSSs would not produce accurate representations of the red sequence and blue cloud. The rest-frame energy range probed by the *R* band at our lowest redshifts, for example, is approximately the same as that probed by the *I* band at the highest redshifts. So, while an $R - I$ versus I CMD would be appropriate for the lower redshifts, we would need to use an $I - Z$ versus Z CMD at higher redshifts.

Ideally, SED fits for each source could be used to estimate rest-frame magnitudes comparable across different redshifts. As described in Section 3.1, we have carried out such fitting for a subset of our sample. However, without rest-frame magnitudes for all sources, we cannot use this method. As a solution to this problem, we created a parametrization of the observed optical magnitude that we could use for our entire sample. We tried several parametrizations and settled upon the following, as the simplest form that gave precise results across the full redshift range:

$$\begin{aligned} f_{\rm blue} &= A_{\rm blue}\,[1 - B_{\rm blue}\,(z - z_0)]\,f_{\nu,R} \\ &\quad + (1 - A_{\rm blue})\,[B_{\rm blue}\,(z - z_0)]\,f_{\nu,I} \\ f_{\rm red} &= A_{\rm red}\,[1 - B_{\rm red}\,(z - z_0)]\,f_{\nu,I} \\ &\quad + (1 - A_{red})\,[B_{\rm red}\,(z - z_0)]\,f_{\nu,Z} \\ M_{\rm red} &= -2.5\log(f_{\rm red}) + 25 - DM \\ M_{\rm blue} &= -2.5\log(f_{\rm blue}) + 25 - DM, \end{aligned}$$

where $A_{\rm blue}$, $B_{\rm blue}$, $A_{\rm red}$, $B_{\rm red}$ and z_0 are the free parameters. To represent the range of galaxies present in our sample, we used four EAZY PÉGASE models for the fitting process: three post-starburst models with ages of 0.1, 0.4 and 5 Gyr, and one constant star-forming model 50 Myr after the inception of star formation with $A_v = 3$. We fit the parametrization by minimizing the combined colour difference between the rest-frame colours and supercolours of all four templates across our entire redshift range. We found

$$\begin{aligned} f_{\rm blue} &= 0.45\,[1 - 1.824\,(z - 0.679)]\,f_{\nu,R} \\ &\quad + 0.55\,[1.824\,(z - 0.679)]\,f_{\nu,I} \\ f_{\rm red} &= 0.424\,[1 - 1.794\,(z - 0.628)]\,f_{\nu,I} \\ &\quad + 0.576\,[1.794\,(z - 0.628)]\,f_{\nu,Z} \end{aligned}$$

to be the best fit. From these equations, we calculated the parametrized absolute magnitudes $M_{\rm blue}$ and $M_{\rm red}$ that we will refer to as the supercolours. These can be thought of as $M_{u^\star}$ and M_B, respectively. To test the accuracy of our parametrization, we can compare $M_{\rm Blue} - M_{\rm Red}$ to $M_{u^\star} - M_B$ for the LSSs where rest-frame magnitudes have been calculated. We find a high degree of concordance: 97 per cent of objects have a difference between these colour measurements under 0.5. 87 per cent have a difference less than 0.25 and 57 per cent have a difference less than 0.1. For our colour analyses, we use these supercolours, except in the case of SC1604, for which we have ACS imaging. Since the ACS imaging is more precise and the central wavelengths are comparable, we adopt those colours for that case.

Fig. 1 shows CMDs for all LSSs in our sample. All spectroscopically confirmed supercluster/cluster members are shown. Diamonds indicate the X-ray AGNs confirmed to be within each LSS via matching to optical sources with high-quality redshifts that are analysed in Section 5. The red sequence for each LSS is delineated by dashed lines. Red sequence fits for each LSS were calculated using a linear fitting and σ-clipping technique. First, a fit to a linear model, of the form

$$C = C_0 + m \times B, \tag{3}$$

where C is either $M_{\rm Blue} - M_{\rm Red}$ or *F606W*−*F814W* and B is either $M_{\rm Red}$ or *F814W* was carried out on member galaxies within a chosen magnitude and colour range using a χ^2 minimization (Gladders et al. 1998; Stott et al. 2009). The fit was initialized with a colour range chosen 'by eye' to conform to the apparent width of the red sequence of the LSS. The magnitude bounds were chosen to be where the red sequence began falling off, whether due to spectroscopic incompleteness or an instrinsic lack of objects, for the entire sample, which we determined as $M_{\rm Red} < -20.9$. In some cases, brightest cluster/group galaxies appearing at bluer colours had to be cut, as well. After the initial fit, the colours were normalized to remove the slope of the red sequence and the resultant colour distribution was then fit to a single Gaussian using iterative 3σ clipping. At the conclusion of the algorithm, the boundaries of the red sequence were defined by a 3σ offset from the centre, except for SC1604. For this supercluster, the colour dispersion was inflated due to the large redshift extent of the LSS and 2σ offsets were used to achieve reasonable boundaries.

While red sequences are well defined for most of our LSSs, the size of the blue cloud varies considerably. We can quantify this by looking at the fraction of blue galaxies for each case. Here, we will define a blue galaxy as one below the lower boundary of the red sequence, including only galaxies with $M_{\rm Red} < -20.9$. The blue fractions for each LSS are displayed in Table 5. Unsurprisingly, two of the highest redshift LSSs, Cl0849 and RXJ1053, have the highest blue fractions. SG0023 and SC1604 have relatively high blue fractions as well, which are probably indicative of actively star-forming galaxy populations. SC1324 has a relatively high blue fraction as well. The other LSSs have lower blue fractions, which may indicate that their populations are more quiescent.

RXJ1716 and RXJ0910 have blue fractions that may be lower than expected, especially considering the high redshift of RXJ0910. Their blue fractions are comparable to the most passive LSS populations, despite their spectral signatures indicating more actively star-forming galaxy populations (see Section 4.2). The issue here may be insufficient completeness in the blue cloud. Indeed, when we include galaxies with only photometric redshifts in calculating the blue fractions, these LSSs have blue fractions of 28 per cent and 35 per cent, respectively (compared to 18 per cent and 26 per cent for the spectroscopic sample). These can be compared to RXJ1757 and RXJ1821, which, as members of the Passive sub-sample, may be expected to have relatively low blue fractions based on their spectral properties. RXJ0910, in particular, should have a higher blue fraction than these two LSSs considering its considerably higher redshift. We do find this to be the case, measuring blue fractions of 28.8 per cent and 27.3 per cent for RXJ1757 and RXJ1821, respectively, when galaxies with only photometric redshifts are included (compared to 16 per cent and 23 per cent for the spectroscopic sample). This implies that RXJ1716 and RXJ0910 have more active star formation than the uncorrected blue fractions in Table 5 suggest.

4.2 Spectral properties

Eventually, we want to learn about the properties of the average AGN host galaxy in each LSS. First, we need a baseline to compare with, which are the average properties of the average galaxy in the overall population. We can accomplish this using co-added

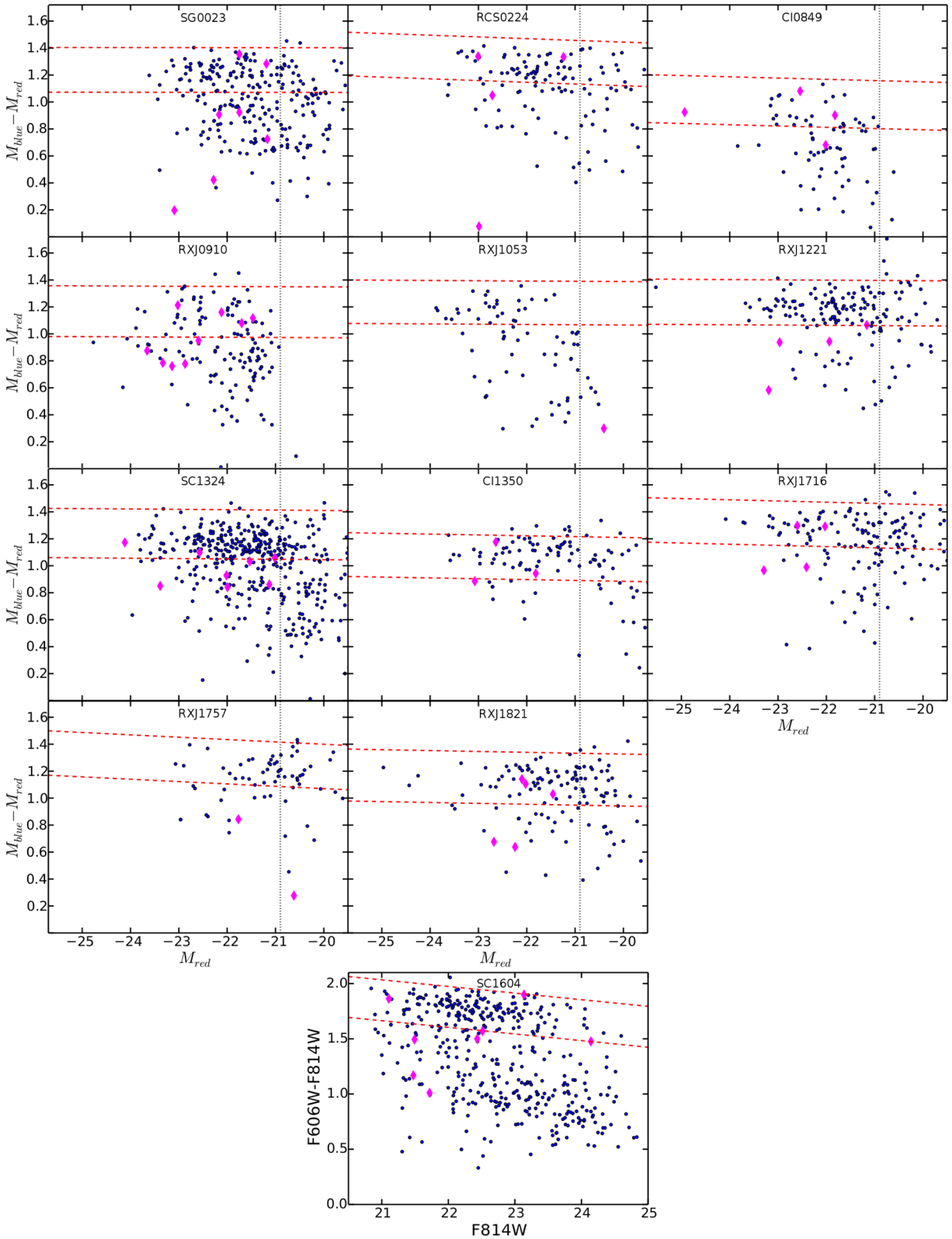

Figure 1. Colour–magnitude diagrams for all LSSs are shown. AGN hosts are shown with magenta diamonds, while all other spectroscopically confirmed LSS members are shown with blue circles. Red dashed lines indicate the extent of the red sequence (see Section 4.1 for more details). Vertical dotted lines indicate the magnitude cut-off used for constructing composite spectra described in Section 4.2. No such line is shown for SC1604 because ACS data were available and so those colours were used to construct the diagrams, although the parametrized colours were used for the magnitude cut-offs for consistency with the other LSSs. For all other LSSs, parametrizations of the *R*, *I* and *Z* bands were used. See Section 4.1 for more details on these parametrizations.

Table 5. LSS average spectral properties and blue fractions

LSS	EW([O_{II}]) (Å)	EW(Hδ) (Å)	$D_n(4000)$	Blue fraction[a]
SG0023	-7.7 ± 0.1	3.0 ± 0.1	1.486 ± 0.002	0.35
RCS0224	-2.2 ± 0.1	1.3 ± 0.1	1.360 ± 0.002	0.27
Cl0849	-11.9 ± 0.3	5.8 ± 0.2	1.213 ± 0.006	0.51
RXJ0910	-8.7 ± 0.1	4.1 ± 0.1	1.382 ± 0.004	0.26
RXJ1053	-5.9 ± 0.2	2.7 ± 0.2	1.541 ± 0.007	0.42
RXJ1221	-1.4 ± 0.1	1.5 ± 0.1	1.638 ± 0.003	0.19
SC1324	-5.3 ± 0.1	2.28 ± 0.04	1.491 ± 0.002	0.32
Cl1350	-1.8 ± 0.1	1.8 ± 0.1	1.546 ± 0.003	0.23
SC1604	-8.2 ± 0.1	3.3 ± 0.1	1.352 ± 0.002	0.38
RXJ1716	-4.1 ± 0.1	2.8 ± 0.1	1.575 ± 0.003	0.18
RXJ1757	-2.0 ± 0.2	1.9 ± 0.1	1.434 ± 0.004	0.16
RXJ1821	-3.1 ± 0.1	2.0 ± 0.1	1.515 ± 0.003	0.23

[a]Blue fraction is defined here as the fraction of galaxies below the bounds of the red sequence and with $M < -20.9$. See Section 4.1 for more details.

spectra, through which we can examine the average star formation and starburst histories of our sample. We co-added all individual spectra, except broad-line AGN, from each LSS into a single composite spectrum, using the cut-off of $M_{Red} < -20.9$ described in Section 4.1, according to the method of Lemaux et al. (2009, 2012). We use three spectral features as our main probes of star formation history: the [O_{II}] doublet, at 3726–3729 Å, the Hδ line, at 4102 and the 4000 Å break. Each of these features probes a different star formation regime. The [O_{II}] emission line is often used as an indicator of current star formation, especially when the Hα line is too redshifted for use, as with optical spectrography (Poggianti et al. 1999). Caution must be exercised when using the [O_{II}] line, since [O_{II}] emission can also be created through low-ionization nuclear emission-line region and Seyfert processes (see, e.g. Yan et al. 2006; Lemaux et al. 2010; Kocevski et al. 2012, Lemaux et al., in preparation).

While populations of young O stars can create strong Balmer and [O_{II}] emission, galaxies with continua dominated instead by older A and B stars tend to exhibit Hδ absorption (Poggianti & Barbaro 1997). Due to the lifetime of these stars, the Hδ line is therefore an indicator of star formation in the past $\sim$1 Gyr. The 4000 Å break, quantitatively measured as $D_n(4000)$, also measures time since the most recent star formation event, as it increases with the mean stellar age (Kauffmann et al. 2003) and is relatively insensitive to changes in dust and stellar-phase metallicity (Lemaux et al. 2012).

Our measurements of $D_n(4000)$ and the [O_{II}] and Hδ equivalent widths[5] for the composite spectra of all LSSs are shown in Table 5. Additionally, these are plotted in Fig. 2. In the left-hand panel, EW([O_{II}]) is plotted versus EW(Hδ). The four regions on the plot, delineated by the vertical line and the upper dashed line, are based on the spectral types of Dressler et al. (1999) and Poggianti et al. (1999), using low-redshift galaxies. Starting from the lower right and moving clockwise, they correspond to star-forming galaxies, quiescent galaxies, post-starburst galaxies and starbursting galaxies. The dashed lines are derived from Dressler et al. (2004) and enclose 95 per cent of normal star-forming galaxies. In the right-hand panel, $D_n(4000)$ is plotted versus EW(Hδ). The shaded regions are areas in this phase space spanned by a range of models derived from Bruzual & Charlot (2003) and Bruzual (2007). The models use either a Salpeter or Chabrier initial mass function, a stellar extinction of $0 \leq Es(B-V) \leq 0.25$ and have stellar-phase metallicites of $Z = 0.4\,Z_{\odot}$, $Z_{\odot}$. The models have either a single burst or a secondary burst of varying intensity. The four different shaded regions represent models with differing times since the last starburst event, shown in the legend.

With these spectral measurements, the LSSs in our sample are differentiated into several sub-samples. The composites of the highest redshift LSSs have the highest average EW([O_{II}]) and EW(Hδ). On average, these LSSs appear to have the highest levels of star formation in our sample and the average member galaxy is likely currently starbursting. This is supported by the $D_n(4000)$ measurements, where the average member galaxies of these LSSs have some of the most recent starburst events. This sub-sample is followed by SG0023 and SC1604 that also appear to have a galaxy population that is star-forming, on average, although at lower levels than the high-redshift sub-sample, and these populations have more recently had starburst events, on average.

RCS0224, RXJ1221, Cl1350, RXJ1757 and RXJ1821 make up a sub-sample of LSSs with quiescent galaxy populations. With the lowest EW([O_{II}]) and EW(Hδ) and the largest $D_n(4000)$ values, the galaxy populations of these LSSs seem to be passive on average and have the least recent starburst events. In an intermediate range are SC1324 and RXJ1716. The average EW(Hδ) measurements for members of these LSSs lie near the boundary between quiescent and star-forming. Additionally, the average time since last starburst appears to be in between those for the actively more actively star-forming SG0023 and SC1604 LSSs and the passive sub-sample of LSSs.

4.3 Summary of global characteristics

Our analysis of the optical colours and average spectral properties suggests that our sample can be roughly broken up into four sub-samples of LSSs that are roughly similar. The highest redshift LSSs in our sample (Cl0849, RXJ0910, RXJ1053) are the bluest and have the most actively star-forming galaxy populations, on average. In fact, significant fractions of actively starbursting galaxies may be present. Hereafter, we will refer to this sub-sample as the High-z LSSs. The galaxy populations of SG0023 & SC1604, similarly, are relatively blue and actively forming stars, on average, although not quite to the extent of the High-z LSSs. While there may appear to

[5] Equivalent widths are measured using the bandpass method. Additionally, EW(Hδ) measurements are corrected for infill.

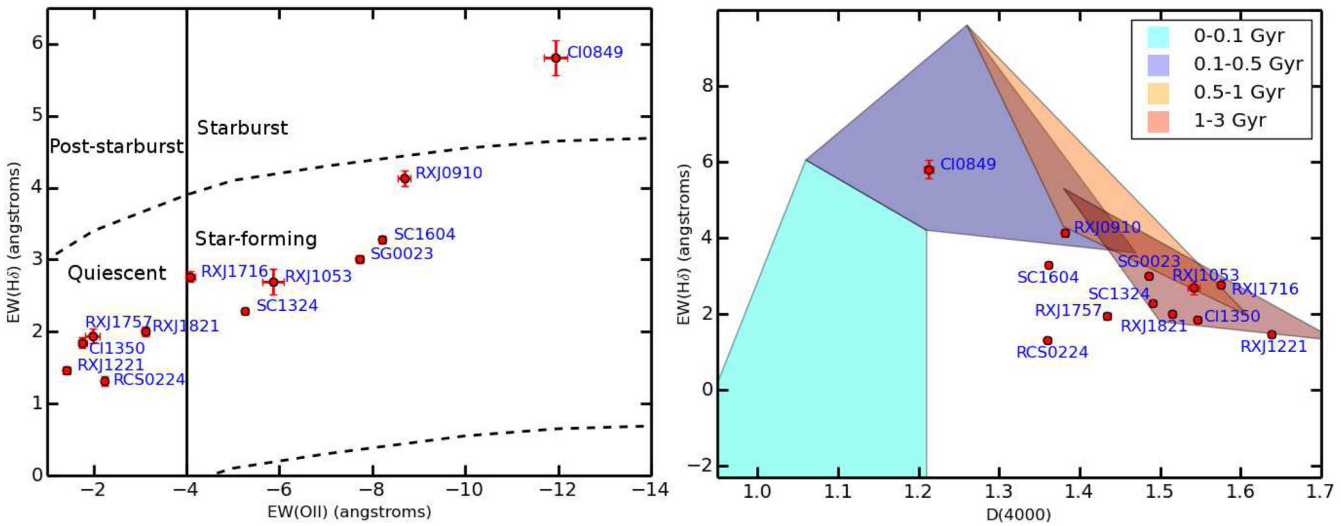

Figure 2. Measurements of spectral features for the composite spectra of each LSS in our sample are shown. Left: EW([O_{II}]) and EW(Hδ) measurements are shown. The four regions on the plot are based on the spectral types of Dressler et al. (1999) and Poggianti et al. (1999), using low redshift galaxies. The dashed lines are derived from Dressler et al. (2004), and enclose 95 per cent of normal star-forming galaxies. *Right*: EW(Hδ) and $D_n(4000)$ measurements are shown. Additionally, regions are plotted that represent a range of post-starburst models derived from Bruzual & Charlot (2003) and Bruzual (2007). The models use either a Salpeter or Chabrier initial mass function, a stellar extinction of $0 \leq Es(B-V) \leq 0.25$, and either stellar-phase metallicities of $Z = 0.4\,Z_{\odot}$, $Z_{\odot}$. Models have either a single burst, with exponential declining star formation ($\tau = 10$ Myr) or include a secondary burst, occurring 2–3 Gyr after the initial starburst event, creating 5–100 per cent of the galaxy's stellar mass or new stars.

be similarities between these sub-samples, our later X-ray analysis shows marked differences between the AGNs in SG0023 & SC1604 and the High-z LSSs, justifying a separate analysis.

Five of the LSSs (RCS0224, RXJ1221, Cl1350, RXJ1757 and RXJ1821) appear to house the most quiescent member populations based on our spectral measurements and they have the lowest blue fractions. We will call this sub-sample the Passive LSSs.[6] This leaves SC1324 and RXJ1716. As mentioned earlier, the spectral properties of these LSSs place their star formation activity at a level higher than the average galaxy in the Passive LSSs, but still lower than SG0023 & SC1604. The higher blue fraction in SC1324 also seems to show that it may have more active star formation than the Passive sub-sample. While RXJ1716 seems to have a rather low blue fraction, correcting for completeness using photometric redshifts implies that it has a blue fraction at least no lower than the Passive sub-sample (see Section 4.1). We analyse SC1324 and RXJ1716 together and refer to them as the Intermediate sub-sample.

5 AGN AND HOST PROPERTIES

Using optical sources with redshifts with quality flags of $Q = 3$ or 4 and the results of our optical matching, we were able to identify X-ray sources that are members of the LSSs in our sample (see Table 3). In total, we find 61 AGNs across all LSSs. 18 of these are in the Passive sub-sample, 12 are in the Intermediate sub-sample, 7 in SG0023, 10 in SC1604 and 14 are in the High-z sub-sample. Note that these numbers include all sources detected at a $>2\sigma$ level in at least one of the three X-ray passbands (see Table 6) and 7 out of the 61 AGNs were detected at lower than the 3σ level.

[6] Note that 'Passive' is used here in a relative sense. The galaxy populations of these LSSs have less star formation activity than the rest of our sample, on average. We do not mean to imply that the average galaxy in these LSSs has negligible star formation.

Additionally, the high levels of X-ray emission ($L_X \gtrsim 10^{42}$ erg s^{-1}) indicate that the detected X-ray sources are unlikely to be anything other than AGN, as star-forming galaxies do not emit at these levels (Ranalli, Comastri & Setti 2003). We also note that our sample, by definition, consists of X-ray-selected AGN, as opposed to AGN in general, because of our selection method. In the following analysis, we refer to X-ray AGN unless where otherwise noted.

5.1 Spatial distribution

Examining the spatial distribution of AGNs located within each cluster can give insight into what processes triggered their nuclear activity. Their positions and characteristics are given in Table 6.

We find AGNs distributed across our LSSs. They are represented in dense cluster cores, in galaxy groups, on the outskirts of groups and clusters, and within the redshift bounds of our LSSs, but not associated with any particular cluster or group. These different regimes can be delineated and analysed using a phase space metric that accounts for separations both on the sky and in radial velocity.

In Fig. 3, we plot $r_{\rm norm} = r/r_{200}$ versus $v_{\rm norm} = |\Delta v|/\sigma_v$ for all spectroscopically confirmed members of our LSSs. Here, r is the projected distance to a group or cluster, while r_{200} is for that same group or cluster, with $r_{200} = 2\sigma_v/(H\sqrt{200})$. Δv is the difference in line-of-sight velocity between that galaxy and a group or cluster, while σ_v is the velocity dispersion for that same group or cluster, calculated within 0.5 Mpc of its centre (see Ascaso et al. 2014 for details on calculating velocity dispersions.). It has been shown that on diagrams such as these, lines of constant $p = r_{\rm norm} \times v_{\rm norm}$, sometimes called caustic lines, are useful for separating out different cluster populations, such as members in the virialized cores and infalling populations (see, e.g. Mamon et al. 2004; Gill, Knebe & Gibson 2005; Haines et al. 2012; Noble et al. 2013). Haines et al. (2012) stacked 30 clusters from the Millenium Simulation, finding that galaxies that had been accreted into the clusters at earlier times,

Table 6. AGN summary

LSS	Num.	RA (J2000)	Dec. (J2000)	z	L_x (soft)[a]	L_x (hard)[a]	L_x (full)[a]	Detection sig.(σ)	p^b	RSO[c]
SG0023	1	00 24 10.9	+04 29 23.5	0.823	6.2	51.0	43.4	12.28	29.67	1.89
SG0023	2	00 24 15.5	+04 23 09.1	0.829	8.3	[d]	19.8	9.64	7.11	−0.71
SG0023	3	00 23 54.9	+04 25 24.6	0.830	0.7	7.1	5.5	3.37	10.41	−0.28
SG0023	4	00 24 09.4	+04 22 41.1	0.841	25.0	36.2	77.1	33.20	0.36	6.28
SG0023	5	00 23 52.2	+04 22 59.8	0.844	25.7	109.8	119.5	50.01	0.20	3.09
SG0023	6	00 23 45.6	+04 22 59.4	0.850	9.7	21.4	37.5	19.84	0.68	4.91
SG0023	7	00 24 07.6	+04 27 26.9	0.854	3.3	[d]	10.5	4.16	12.36	2.00
RCS0224	1	02 24 36.9	−01 53 56.5	0.774	7.8	25.4	30.6	45.19	0.19	7.68
RCS0224	2	02 24 38.2	−01 53 49.7	0.778	0.8	[d]	2.1	3.13	0.01	−0.11
RCS0224	3	02 24 37.3	−01 55 02.4	0.778	0.2	29.2	11.5	24.68	0.02	1.66
RCS0224	4	02 24 39.8	−01 54 30.7	0.781	0.8	2.4	3.5	5.20	0.20	−0.22
Cl0849	1	08 49 04.1	+44 56 47.3	1.263	1.3	16.0	10.5	9.79	0.62	0.49
Cl0849	2	08 48 58.8	+44 56 21.8	1.263	1.8	9.8	10.5	10.21	0.58	0.53
Cl0849	3	08 49 05.3	+44 52 04.4	1.265	2.1	56.7	31.9	24.50	2.28	1.74
Cl0849	4	08 49 03.9	+44 50 25.2	1.274	1.2	11.3	8.7	6.19	4.87	−0.48
RXJ0910	1	09 10 40.9	+54 20 08.8	1.096	[d]	10.9	4.9	6.06	0.99	2.15
RXJ0910	2	09 10 48.2	+54 22 30.0	1.097	1.0	[d]	3.8	4.35	0.19	−0.25
RXJ0910	3	09 10 42.8	+54 20 11.0	1.099	0.7	7.4	5.1	6.57	0.52	0.24
RXJ0910	4	09 09 54.0	+54 17 55.1	1.101	[d]	22.7	13.3	8.10	0.45	1.54
RXJ0910	5	09 10 34.9	+54 24 54.9	1.102	1.0	[d]	2.7	2.79	0.14	0.01
RXJ0910	6	09 09 55.7	+54 18 14.6	1.102	2.5	20.7	16.5	10.68	0.01	2.02
RXJ0910	7	09 09 45.2	+54 16 33.9	1.105	[d]	13.4	7.7	3.34	1.84	1.13
RXJ0910	8	09 10 42.8	+54 20 37.2	1.106	0.7	8.2	6.7	8.38	0.65	2.05
RXJ0910	9	09 10 04.9	+54 17 36.6	1.117	1.0	[d]	5.2	3.52	3.77	0.44
RXJ1053	1	10 53 39.6	+57 36 48.6	1.125	1.8	[d]	5.5	4.99	5.23	5.77
RXJ1221	1	12 21 51.4	+49 19 29.7	0.692	1.2	9.1	7.6	8.16	3.55	1.72
RXJ1221	2	12 21 49.0	+49 12 49.0	0.696	0.4	2.9	2.4	3.33	1.37	3.88
RXJ1221	3	12 21 00.9	+49 20 38.7	0.698	[d]	18.1	8.9	7.98	1.23	1.76
RXJ1221	4	12 21 56.1	+49 13 45.7	0.699	[d]	5.9	3.0	3.67	0.25	0.97
SC1324	1	13 24 51.5	+30 12 42.6	0.660	1.1	[d]	2.2	2.51	7.48	2.12
SC1324	2	13 24 36.6	+30 23 17.4	0.662	1.1	8.0	6.8	4.28	27.25	2.02
SC1324	3	13 24 38.6	+30 58 08.3	0.676	2.8	[d]	7.6	5.20	5.49	2.15
SC1324	4	13 24 52.9	+30 52 18.0	0.697	1.3	[d]	3.0	2.64	0.97	1.67
SC1324	5	13 24 52.0	+30 50 51.5	0.700	[d]	13.2	6.6	6.47	4.30	1.09
SC1324	6	13 24 50.6	+30 56 24.2	0.702	0.7	5.7	4.2	3.10	1.49	0.36
SC1324	7	13 25 08.7	+30 52 13.5	0.757	1.5	[d]	4.4	2.69	2.15	0.94
SC1324	8	13 24 28.8	+30 53 19.5	0.778	1.5	[d]	4.4	2.62	51.71	0.75
Cl1350	1	13 49 34.4	+60 02 28.1	0.798	2.6	65.6	38.5	12.95	1.09	1.11
Cl1350	2	13 50 46.0	+60 07 00.9	0.802	[d]	18.0	10.5	7.01	0.04	0.71
Cl1350	3	13 50 50.1	+60 08 03.3	0.807	2.2	3.8	7.4	5.21	0.34	−0.69
SC1604	1	16 04 23.9	+43 11 25.8	0.867	12.7	24.1	47.2	28.11	0.63	4.30
SC1604	2	16 04 25.9	+43 12 45.3	0.871	6.3	11.3	21.1	11.78	1.02	1.42
SC1604	3	16 04 24.0	+43 04 35.1	0.899	[d]	[d]	5.9	2.21	0.07	−0.11
SC1604	4	16 04 15.6	+43 10 16.6	0.900	17.2	37.5	62.7	13.16	1.55	1.76
SC1604	5	16 04 37.7	+43 08 58.0	0.900	1.1	6.5	6.2	3.02	1.59	[e]
SC1604	6	16 04 06.1	+43 18 07.7	0.913	13.4	27.7	45.8	22.64	2.31	0.99
SC1604	7	16 04 36.7	+43 21 41.1	0.923	6.3	19.4	26.5	10.50	0.04	3.52
SC1604	8	16 04 01.4	+43 13 51.1	0.927	11.2	31.8	44.8	19.32	0.97	[e]
SC1604	9	16 04 05.2	+43 15 20.8	0.934	3.2	[d]	10.3	5.12	0.00	1.01
SC1604	10	16 04 10.9	+43 21 11.2	0.935	1.1	11.9	8.9	3.50	0.13	−0.97
RXJ1716	1	17 16 37.8	+67 07 30.3	0.805	2.7	5.3	9.2	5.26	0.40	0.09
RXJ1716	2	17 17 03.9	+67 08 59.2	0.809	[d]	7.9	5.1	3.68	0.14	2.14
RXJ1716	3	17 16 24.4	+67 05 28.6	0.816	[d]	9.9	4.9	2.44	0.74	1.95
RXJ1716	4	17 16 41.9	+67 06 07.0	0.821	[d]	8.2	5.7	3.06	0.97	0.09
RXJ1757	1	17 57 25.2	+66 31 50.7	0.693	2.2	7.1	8.7	7.17	0.03	2.57
RXJ1757	2	17 57 07.5	+66 30 18.6	0.707	2.5	4.1	8.4	6.97	4.68	5.89
RXJ1821	1	18 21 07.7	+68 23 39.3	0.813	2.1	[d]	6.2	2.76	0.73	0.04
RXJ1821	2	18 21 36.6	+68 30 02.1	0.814	3.2	[d]	9.1	5.46	0.27	2.65

Table 6 – *continued*

LSS	Num.	RA (J2000)	Dec. (J2000)	z	L_x (soft)[a]	L_x (hard)[a]	L_x (full)[a]	Detection sig.(σ)	p^b	RSO[c]
RXJ1821	3	18 21 02.8	+68 25 07.3	0.820	1.2	10.7	8.7	4.62	0.48	2.47
RXJ1821	4	18 21 23.9	+68 26 32.9	0.822	2.0	[d]	7.7	4.42	0.37	0.59
RXJ1821	5	18 21 27.0	+68 32 34.7	0.824	8.2	14.1	25.9	12.15	1.40	0.22

[a]Rest-frame X-ray luminosity in units of 10^{42} erg s^{-1}. Soft, hard and full bands are defined as 0.5–2.0, 2.0–7.0 and 0.5–7.0 keV, respectively.
[b]Phase space metric, defined in Section 5.1 as the product of the scaled distances on the sky and in velocity space to the nearest group or cluster.
[c]Scaled offset from the centre of the red sequence fit in units of red sequence half-widths. Refer to Sections 4.1 and 5.2.
[d]Undetected in respective band.
[e]Red sequence offsets for SC1604 AGN hosts were only calculated for those with ACS imaging.

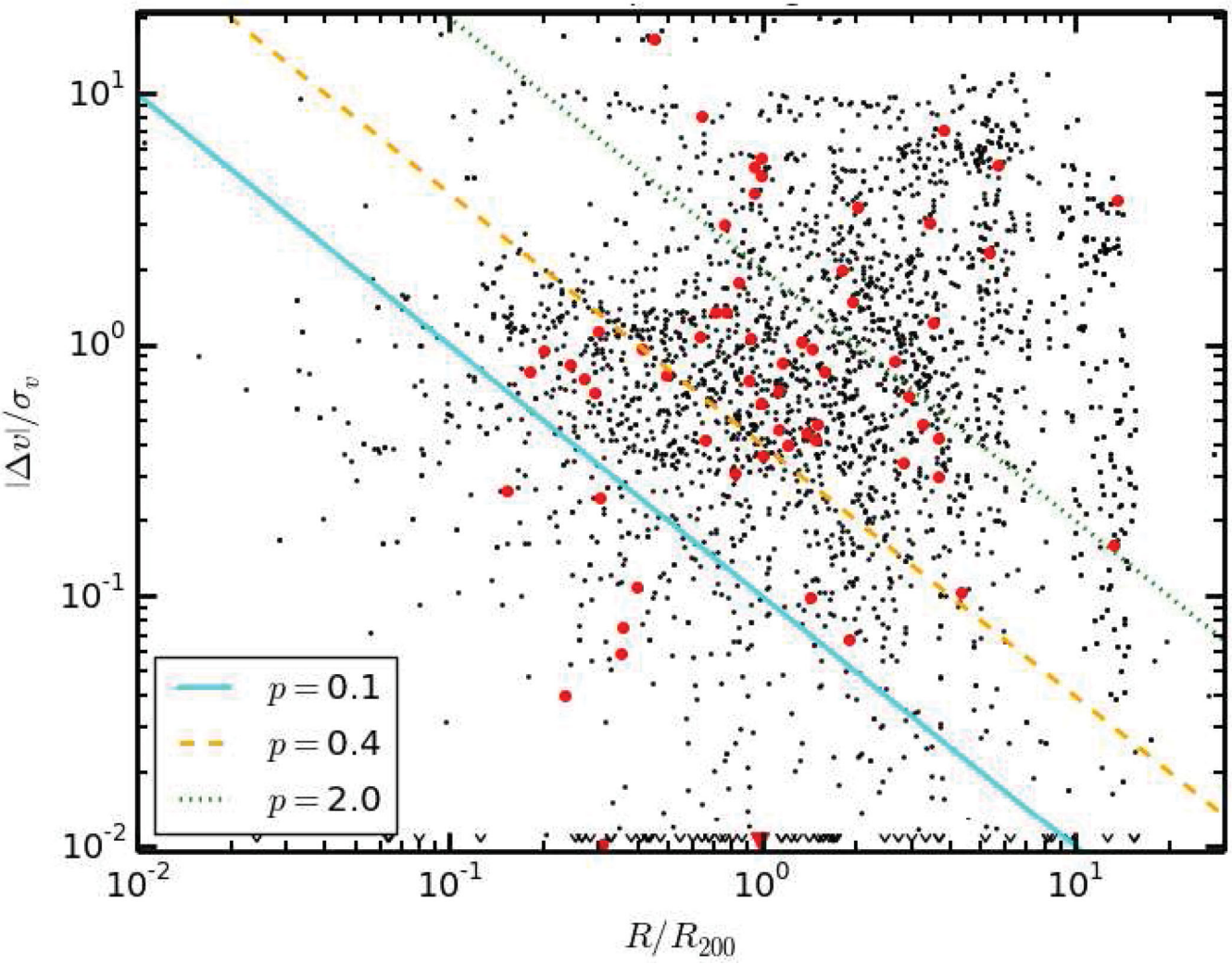

Figure 3. For each point, distance to the nearest cluster is plotted on the sky versus the difference in radial velocity. The nearest cluster is defined as the one with the lowest value of $r/r_{200} \times |\Delta v|/\sigma_v$. See Section 5.1 for more details. AGNs are plotted with larger circles, while all spectroscopically confirmed members of LSSs in our sample are plotted with smaller circles. AGNs and all sources that lie below the field of view of the plot are shown at the bottom with triangles and carets, respectively. Note that these do not represent upper limits, but instead are points with very small, but well-defined values of $|\Delta v|/\sigma_v$ that are difficult to plot in log-space. Three lines of constant $p = r/r_{200} \times |\Delta v|/\sigma_v$ are plotted.

which should include mostly galaxies in the cluster cores, tended to be located inside caustic lines with lower values of p, while those accreted at later times, which should include infalling populations, were located outside caustic lines, having higher values of p.

For each galaxy, p must be calculated relative to a specific group or cluster. Since our sample contains a substantial subset of galaxies that are not close to any group or cluster, it is not always clear that which object should be used for these references. To determine which group or cluster should be used for reference, p was calculated for each galaxy relative to all groups and clusters, and the smallest value for p was retained.

In Fig. 3, lines corresponding to $p = 0.1$, 0.4 and 2 are plotted. As in Noble et al. (2013), galaxies with $p < 0.1$ are likely in a dense cluster or group core and have had time to viriliaze, while those with

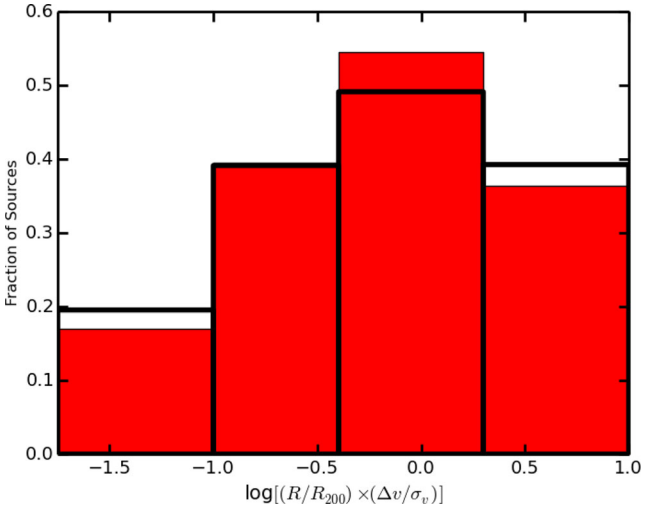

Figure 4. Plotted are histograms of $p = r/r_{200} \times |\Delta v|/\sigma_v$ for AGNs (filled bars) and all spectroscopically confirmed members of LSSs in our sample (unfilled bars). For more details on how p is measured, see Section 5.1. The four bins are separated by the same lines of constant p as plotted in Fig. 3, at $p = 0.1$, 0.4 and 2.

$p > 0.4$ (and, in our case, <2) are likely part of recently accreted infalling populations. The region $0.1 < p < 0.4$ is an intermediate region. Because of our different scope (we include a substantial number of galaxies in our sample at larger spatial and/or velocity distances from the nearest group or cluster), we also include the caustic line at $p = 2$. Galaxies with $p > 2$ are likely not associated with any group or cluster. In Fig. 4, we plot the fraction of galaxies in each of the four regions created with our three caustic lines. The distributions are shown for all spectroscopically confirmed galaxies and for just the X-ray sources. We can see that the distributions look similar, which is confirmed by a KS test. This suggests that AGNs follow the overall distribution of galaxies with respect to groups and clusters. This implies that triggering mechanisms are at most weakly dependent on global environment, at least in relation to the four regimes probed here: dense cluster cores, intermediate regions, infalling populations and our 'superfield' populations ($p > 2$) not associated with any particular group or cluster.

5.2 AGN host galaxy colours

Fig. 1 presents CMDs that are described in Section 4.1, for all LSSs. Confirmed AGN members of the LSSs are shown with red diamonds. While many AGN hosts lie on the red sequence, there are also a number just below it, in the green valley. Generally, the green valley is sparsely populated compared to the red sequence and blue cloud and may be a transitional region where blue galaxies are evolving on to the red sequence (Faber et al. 2007). Previous work, including Kocevski et al. (2009), Rumbaugh et al. (2012) and a number of wide-field surveys (Sánchez et al. 2004; Nandra et al. 2007; Georgakakis et al. 2008; Silverman et al. 2008), has found an association between active galaxies and the green valley. While an association with this region could have a number of different implications, we examined colour offsets of the AGN hosts from the red sequence to quantify this association.

To calculate red sequence offsets (RS offsets), we used the fits to the CMDs described in Section 4.1. For a given galaxy, the RS offset is defined as the vertical distance above the centre of the red sequence, divided by the half-width of the red sequence. The

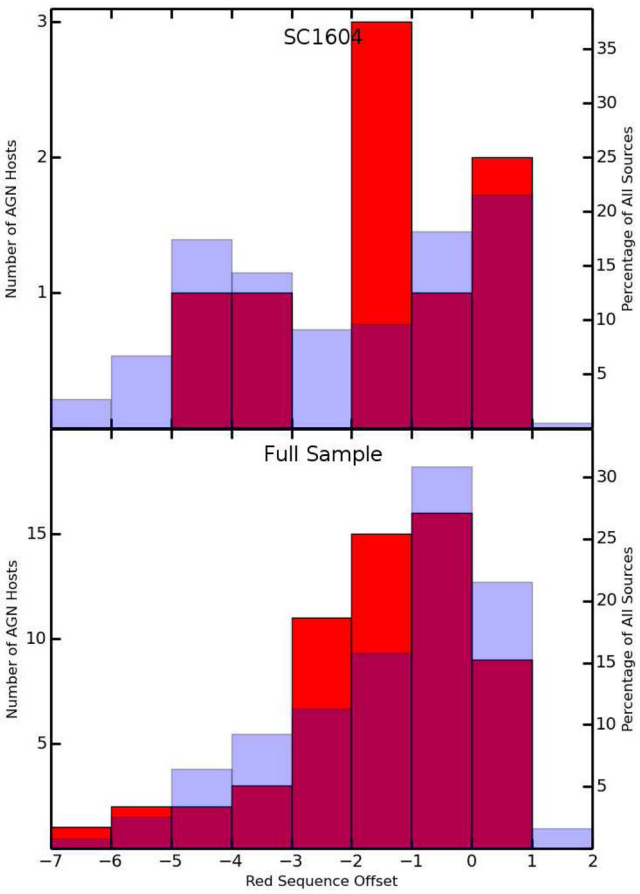

Figure 5. Histograms of the RS offsets are shown. The RS offset is defined as the distance below the centre of the red sequence on a CMD, divided by half the width of the red sequence. The red histograms show the number of AGN hosts, while the lighter, blue, transparent histograms show the distributions for all spectroscopically confirmed member galaxies in our sample. The top plot shows the distributions for just the SC1604 LSS, while the bottom plot shows the distributions for the full sample (including SC1604). The red sequence, green valley and blue cloud approximately correspond to RS offsets of $-1 < \Delta RS < 1$, $-3 < \Delta RS < -1$, $\Delta RS < -3$ on these plots.

half-width is defined here as the vertical distance from the centre of the red sequence to its boundary, so the red sequence ranges from an RS offset of −1.0 to 1.0. Histograms of RS offsets are shown in Fig. 5. The top panel shows only SC1604, while the bottom panel shows all LSSs (including SC1604). For SC1604, the CMDs were constructed using ACS colours.[7] Since ACS data were only available for SC1604, the other diagrams were constructed using our so-called supercolour parametrization of the *R*, *I* and *Z* colours, described in Section 4.1. The RS offsets therefore use the ACS colours for SC1604 and the supercolours for all other LSSs. Because SC1604 used a different colour scheme and it has a very well-defined blue cloud unlike many other members of our sample, we plot it by itself in the top panel of Fig. 5. The nature of the RS offsets allows us to easily compare the different colour

[7] Note that the ACS spatial coverage is smaller than the LFC coverage, meaning that two of the SC1604 AGNs are not included in our colour analyses. We do not expect the omission of these two AGNs to significantly affect our results, as these two excised AGNs did not have exceptional X-ray luminosities or LFC colours compared to the other SC1604 AGNs.

Table 7. AGN hosts' average spectral properties.

Sub-sample	EW([O_{II}])	EW(Hδ)	$D_n(4000)$
Passive	-7.1 ± 0.3	2.8 ± 0.2	1.30 ± 0.01
Intermediate	-8.4 ± 0.4	5.3 ± 0.2	1.5 ± 0.01
SG0023+SC1604	-8.0 ± 0.2	1.0 ± 0.2	1.21 ± 0.01
High-z	-12.2 ± 0.5	6.6 ± 0.4	1.21 ± 0.01

schemes and the different LSSs with different red sequence fits. In the bottom panel of Fig. 5, we plot the RS offsets for all of our sample, including SC1604. For both plots, the distribution of AGN hosts only is shown with the darker red histograms. All other spectroscopically confirmed members of the LSSs are shown with the blue, lighter, transparent histograms. For the AGN hosts, the number in each bin are plotted, as shown on the left axes. For all LSS members, the percentage in each bin is shown on the right axes. The AGN histograms are scaled so that both the left and right y-axis labels apply.

In the top plot, we can see that the overall galaxy population in SC1604 is bimodal: it has a well-formed blue cloud and red sequence, with associated peaks in the RS offset, with a trough in between, which represents the green valley. From this plot, the approximate area of the green valley is a RS offset between -3 and -1. In SC1604, 38 per cent of AGN hosts lie in this region, while only 19 per cent of the rest of the galaxies do. This is a marked difference, although the small number of AGNs means that it is not significant.

In contrast, looking at our entire sample in the bottom plot, there is no bimodality in the overall galaxy distribution. This is likely because many of the LSSs in our sample do not have well-formed blue clouds, meaning that we see no peak at lower RS offsets values as in the SC1604 distribution. However, AGNs still appear to be overrepresented just below the red sequence. For SC1604, the green valley appeared to be between a RS offset of -3 and -1. If we consider this same region, we have 44 per cent of the AGN population and only 27 per cent of the overall population. While a KS test finds that the two distributions in the lower plot differ at less than a 90 per cent confidence level, the results are still suggestive of a link between the green valley region and AGN activity.

5.3 Spectral analysis of AGN hosts

To investigate the connection between AGN activity and star formation, we created composite spectra of the AGN hosts, as in Section 4.2. The spectra for all AGNs (with $L_x > 10^{42.5}$erg s^{-1}, see Sections 5.5 and A1) in each of the four sub-samples (Passive-, Intermediate- SG0023+SC1604 and High-z) were co-added into a composite spectrum. These co-additions are necessary because of the small number of AGNs in most LSSs. Measurements of the spectral features of each of the four composite spectra are shown in Table 7. In addition, the EW(Hδ) and $D_n(4000)$ values are plotted in Fig. 6, along with evolutionary tracks for post-starburst galaxies described in Section 4.2.

All four sub-samples have significant [O_{II}] emission. While [O_{II}] emission can be used as a proxy for ongoing star formation, in all cases, it is likely that most or a significant portion of this emission is from the AGNs themselves. Because of this likely contamination of the EW([O_{II}]) measurements from AGNs, we are unable to use it for the analysis of the AGN hosts.

As described in Section 4.2, the Hδ line can be used as a proxy for recent star formation, as it tracks the A and B stellar population.

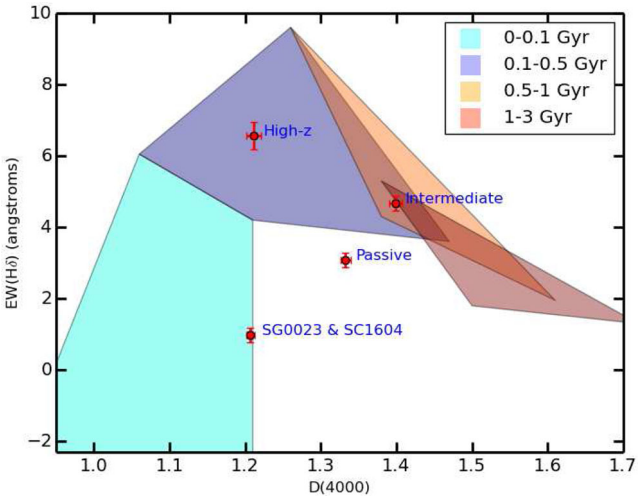

Figure 6. EW(Hδ) and $D_n(4000)$ measurements are plotted against each other for the composite spectra composed of the AGNs in each of the Passive-, Intermediate- and High-z sub-samples and SG0023 & SC1604. Additionally, the evolutionary tracks for post-starburst galaxies based on a range of models and initial parameters are displayed. The legend notes the time since last starburst event for galaxies in each region. See Section 4.2 for more details.

While strong Hδ absorption indicates recent star formation, weak absorption can indicate either an older stellar population where A and B stars have died out or a very young population dominated by O stars. Analysis in conjunction with the 4000 Å break can break this degeneracy, as a larger $D_n(4000)$ measurement correlates with an older stellar population. If we examine Fig. 6, we see the average AGN host in SG0023 & SC1604 has little Hδ absorption and a low $D_n(4000)$ measurement. This places the average host in these LSSs near the beginning of the post-starburst evolutionary tracks, meaning a starburst event is either ongoing or has just ended. This is consistent with the relatively blue colours and star formation activity in the average galaxy in the overall populations, although the AGN hosts are much more active.

The AGN hosts in the High-z sub-sample have a higher average EW(Hδ) than for SG0023 & SC1604, although the value of $D_n(4000)$ is the same within the uncertainties. The average High-z host has had a starburst within the last 100–500 Myr, according to these measurements. This is less time than the average galaxy in the overall population of these LSSs, although it is only about equal to Cl0849 that appears to be the most actively star-forming LSS in our sample. We see a similar trend for the Intermediate and Passive AGN hosts. In both cases, the average AGN host in these sub-samples has a larger EW(Hδ) and a smaller $D_n(4000)$. At this point on the evolutionary tracks, this indicates a more recent starburst event.

We can conclude that in all cases, the average AGN host has more recently had a starburst event than the overall galaxy population. However, the degree of the difference between the AGN population and the overall population in SG0023 and SC1604 is remarkable when compared with the other LSSs. When comparing the average AGN population spectral properties for the High-z, Intermediate and Passive sub-samples in Fig. 6 to those of the overall galaxy populations of their substituent LSSs in Fig. 2, we can observe that the AGN populations occupy a space that represents modestly younger stellar populations. But the AGNs in SG0023 and SC1604 appear to have much younger stellar populations than their overall galaxy population in comparison. While the High-z sub-sample had

Table 8. Close kinematic pairs.

Sub-sample	Num. of AGNs with CKP	Perc. of AGNs with CKP	Perc. of all Gal. with CKP
Passive	2	11 ± 7	11 ± 2
Intermediate	1	8 ± 11	15 ± 2
SG0023+SC1604	6	35 ± 10	21 ± 2
High-z	2	14 ± 7	6 ± 2
Field	8	9.5 ± 3	6.7 ± 0.6

the most recent starburst events, on average, among the overall populations, SG0023 and SC1604 have leap-frogged into the position of most recently star-bursting when considering the average AGN host populations. They have considerably more recent, or even ongoing, star formation compared to the High-z AGN sample. This suggests that there is something exceptional about the AGN in the SG0023 and SC1604 sub-sample.

5.4 Close kinematic pairs

To investigate a connection between AGN triggering and galaxy interactions, we can locate close kinematic pairs (CKPs) that we define as two galaxies within 70 h^{-1} kpc on the sky and within 350 km s^{-1}, typical values for identifying close pairs (Ssee, e.g. Nazaryan et al. 2014; Robotham et al. 2014; Barrera-Ballesteros et al. 2015; Wisnioski et al. 2015; Contini et al. 2016), using our spectroscopic sample. While galaxies that have recently undergone a merger may not have a CKP, as the two galaxies may have coalesced, or they may still be too close together to resolve, galaxies that have recently had a more minor interaction should be more likely to lie in close proximity, as should galaxies that will soon undergo interactions. While this analysis cannot tell us which specific galaxies have recently merged or interacted, it can tell us which LSSs have galaxy interactions happening more frequently, since their galaxy populations should have more pairs of galaxies either about to undergo interactions or having recently undergone interactions that did not result in coalescence and thus appearing as CKPs. In short, CKP fraction is a proxy here for how likely the average galaxy in an LSS is to have recently undergone a merger, even though we cannot tell if an individual AGN host has recently interacted.

The percentages of AGNs and all spectroscopically confirmed galaxies in each sub-sample with CKPs are shown in Table 8. Uncertainties were calculated using MC simulations, where a simple model was used with a flat percentage chance to discover a CKP in each case. Estimated uncertainties were weakly dependent on this discovery rate and completeness. Although only a handful of AGN hosts in our sample have a CKP, SG0023 & SC1604 have large fractions of AGN hosts with CKPs. At 35 per cent of the AGN population in these LSSs, this is over twice the percentage of AGNs with CKPs in any of the other three sub-samples. In fact, at 21 per cent, the fraction of CKPs in the overall galaxy population in SG0023 & SC1604 is the highest out of our sample,[8] as well. Also, while the low number of AGNs in our LSSs means that the fraction with CKPs has a high uncertainty, the combined fraction of AGNs in the Passive-, Intermediate- and High-z sub-samples is more precise and is still only 11 per cent, considerably lower than for SG0023 & SC1604.

[8] Our photometric redshift catalogues predict that relatively few CKPs have been missed due to incompleteness, so this is unlikely to be the cause of the differences observed in Table 8.

In addition to comparing between our sub-samples, we can also look at the field galaxies in our sample. For this analysis, we considered a field galaxy to be anywhere outside the redshift bounds of our LSSs, but still within the overall redshift bounds of our sample ($0.65 < z < 1.28$). The fraction of CKPs in this sample is relatively low, as shown in Table 8, with only 9.5 per cent of the AGN population and 6.7 per cent of the overall population having CKPs. This is unsurprising, since the less dense field environment should be less conducive towards galaxy interactions. And again, while our sample is small, the CKP fraction is not significantly higher for the combined AGN population of the Passive-, Intermediate- and High-z sub-samples than for the field galaxies. For the overall populations, the passive- and High-z sub-samples also do not have CKP fractions higher than that for the overall field population at the 3σ level.

On the other hand, the relatively large number of AGN hosts with CKPs in SG0023 & SC1604 are likely related to the large fraction of CKPs in their overall populations. Notably, the AGN hosts in these LSSs are alone in having a CKP fraction significantly above zero. While small number statistics make the comparison to the other LSS AGN populations somewhat uncertain, these results suggest that the AGN population in SG0023 & SC1604 is influenced by a higher rate of galaxy interactions among their hosts.

5.5 X-ray Luminosity

In this section, we examine the differences in the X-ray luminosities of the AGN populations in our sample. We calculate rest-frame luminosities for X-ray point sources with known redshifts, using a power-law spectral model with a photon index of $\Gamma = 1.4$, described in Section 3.

X-ray luminosities for all member AGNs are listed in Table 6 and the full-band luminosities are displayed in the left-hand panel of Fig. 7. Objects with luminosities below $10^{42.5}$ erg s^{-1} were cut from the sample because of low completeness in this regime and the lighter bars in the histogram represent corrections for completeness. See Section A1 for more details. The luminosity distributions for the Passive-, Intermediate- and High-z sub-samples all peak in the lowest luminosity bin, falling off sharply towards the highest bin, especially the Intermediate sub-sample that only has AGNs in the lowest luminosity bin. The luminosity distribution for SG0023 & SC1604 is noticeably different from that of the rest of the AGNs, peaking at high luminosity in contrast to the other sub-samples. These LSSs have a disproportionate number of AGNs with high luminosities, containing 8 out of the 10 AGNs with luminosities above $10^{43.5}$ erg s^{-1}. The difference between the distributions is confirmed by a KS test at the 3σ level, when comparing the SG0023 & SC1604 to the distribution of all other AGNs. Although correcting for our X-ray luminosity limits, as discussed in Section A1, does slightly alleviate the discrepancy; it does not explain the discrepancy. With these corrections, a KS test finds the SG0023 & SC1604 luminosity to be different from the other sub-samples at the $\gtrsim$97 per cent level.

These discrepancies could also be caused by spectroscopic incompleteness. It is possible that bluer, more luminous AGN hosts were missed if redder galaxies evaluated to be more likely to reside in the LSSs were preferentially targeted in our slit masks instead. To estimate the number of galaxies complete spectroscopy would add, we use our photometric redshift catalogues, although we can only perform the analysis for a subset of our sample as photometric redshifts have only been calculated for SG0023, RXJ0910, SC1324, SC1604, RXJ1716, RXJ1757 and RXJ1821 so far. For each X-ray point source matched to a galaxy in our photometric catalogue

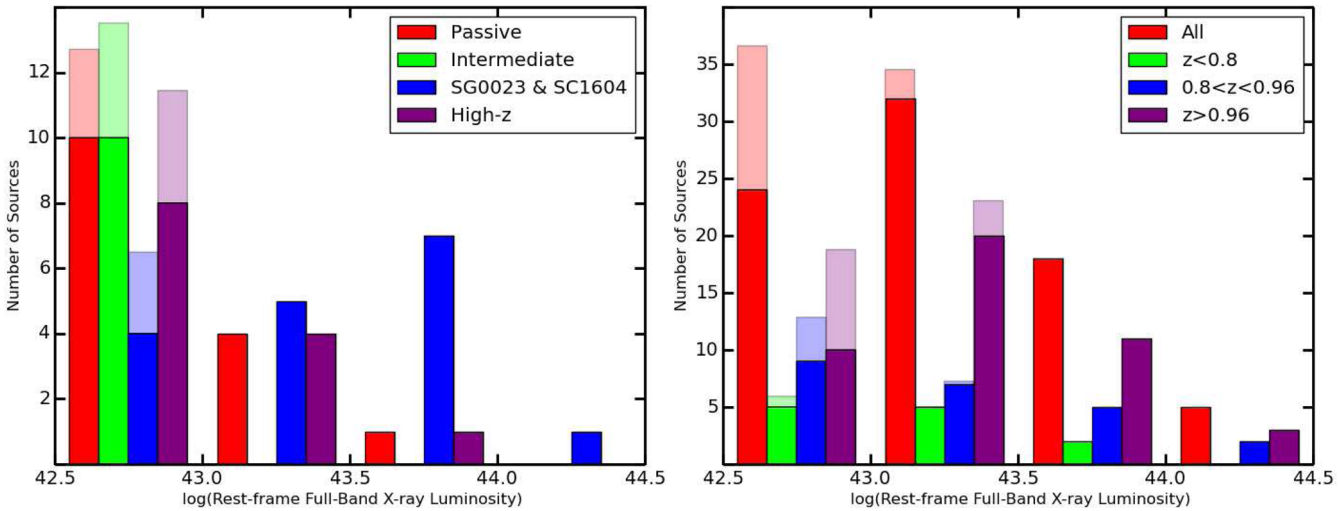

Figure 7. Histograms of the rest-frame, full-band X-ray luminosities of AGNs in our sample are shown. The x-axis is in log-space, representing $\log(L_x)$. In the left-hand panel, luminosities are shown for all AGNs within the LSSs in our sample, sub-sampled as described in Section 4.3. In the right-hand panel, the luminosities for field galaxies in our sample are shown. See Section 5.4 for a description of their selection. In both plots, corrections for the X-ray luminosity limits are shown with lighter bars. See Section A1 for details about these completeness calculations.

without a high-quality redshift in the fields of view of these *Chandra* observations, we estimated the probability that source was within the redshift range of the respective LSS (See Section A2 for more details). Ignoring objects with less than a 5 per cent chance of membership, we estimate that 0.2, 1.7, 0, 0, 0.8, 0 and 0.2 sources would be added in SG0023, RXJ0910, SC1324, SC1604, RXJ1716, RXJ1757 and RXJ1821, respectively, with complete spectroscopy. Because these estimates are small (increasing our sample size, on average, by ∼10 per cent), it is unlikely that spectroscopic completeness is causing any discrepancies between the luminosity distributions of our sub-samples.

In the right-hand panel of Fig. 7, we plot the X-ray luminosities for the field galaxies in our sample, as defined in Section 5.4. Again, the lighter bars in the histogram represent corrections for completeness. These AGNs are binned by redshift to roughly correspond to the redshifts of the sub-samples we made for our LSS AGNs. The redshift range $0.8 < z < 0.96$ roughly corresponds to the combined redshift range for SG0023 & SC1604. Most of the galaxies in the passive sub-sample are at $z < 0.8$, while only the galaxies in the High-z sub-sample have redshifts greater than 0.96.

Both similarities and differences can be seen between the field and LSS AGN luminosity distributions. The $z < 0.96$ field AGN luminosity distributions, like all of those for the LSS AGNs except SG0023 & SC1604, peak in the lowest luminosity bin and fall off those higher luminosities, although they do not appear to fall off as quickly. The $z > 0.96$ field AGN luminosity distribution peaks in the second lowest luminosity bin, unique among populations studied here, and this does not appear to be a product of lower luminosity limits at higher redshifts. A KS test finds that the $z > 0.96$ field distribution differs from the $z < 0.8$ and $0.8 < z < 0.96$ field AGN distributions at the 94 per cent and 89 per cent levels, approximately. The $z > 0.96$ field AGN luminosity distribution is also found to differ from the Passive-, Intermediate- and High-z sub-samples at the 3σ level by a KS test. KS tests find that the intermediate distribution is likely to be different from all field distributions at the 99 per cent level, in fact, although this is probably related to the peculiar absence of $L_x > 10^{43}$ erg s^{-1}AGNs in these LSSs. None of the other sub-sample luminosity distributions are found to vary from those of the $z < 0.96$ field at a significant level. Additionally, since the SG0023 & SC1604 distribution was found to be different from the other LSS luminosity distributions, but was not found to be significantly different from any of the field distributions, this suggests that the field AGN luminosity distributions are partway between those of SG0023 & SC1604 and the other sub-samples.

There appear to be more luminous AGNs in the field than in the LSSs, excluding SG0023 & SC1604. More luminous AGNs could be the result of larger reservoirs of cold gas available in field AGNs, which is expected, given that field galaxies tend to be bluer.[9] This could also explain the higher luminosity of the $z > 0.96$ field AGNs compared to those at lower redshifts, as the blue fraction for galaxies tends to increase with redshift. Because of the low CKP fractions in the field populations, even at high redshift, it is unlikely that the mechanisms that create high-luminosity AGNs in SG0023 & SC1604 are doing the same in the field. The marked difference between the SG0023 & SC1604 luminosity distributions and those of the other LSS AGNs and, to a lesser extent, those of the field AGNs suggests that different triggering mechanisms may be taking precedence, which was also indicated by the CKP fractions.

5.5.1 Relation to host colours and spectroscopy

In the left-hand panel of Fig. 8, we plot the full-band, rest-frame X-ray luminosities versus the RS offsets, as described in Section 5.2. We have divided the plot into six regions based on X-ray luminosity and RS offsets. The x-axis is broken up into three regions, delineating, from left to right, the blue cloud, green valley and red sequence. On the y-axis, we break up the plot into two sections based on luminosity, separating AGNs at $L_x = 10^{43.3}$ erg s^{-1}. This boundary was chosen in Rumbaugh et al. (2012) and kept for ease of comparison to that work. Almost all of the red sequence AGNs lie below this line and most of the blue cloud AGNs lie above it. This result is unsurprising, since red sequence AGN hosts should have smaller reservoirs of cold gas for fuel and should tend to house lower luminosity AGNs, while the opposite would be expected in the blue

[9] Indeed, we find that field AGN at $z < 0.96$ and $z > 0.96$ have median $M_{\rm Blue} - M_{\rm Red}$ values 0.21 and 0.13 mag bluer than LSS AGN at the same redshifts for our sample.

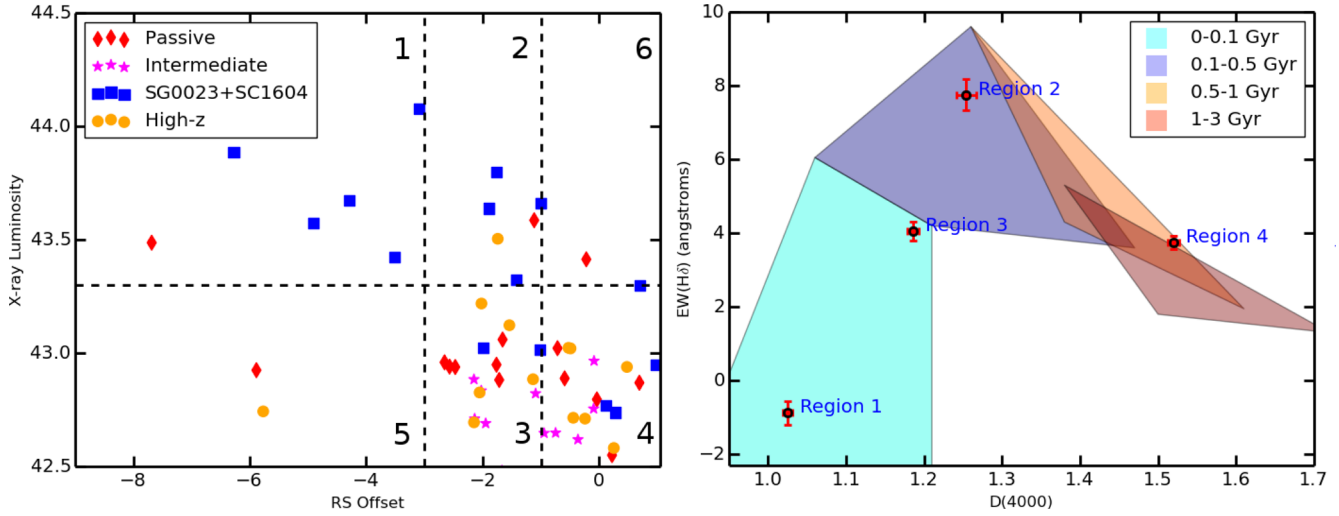

Figure 8. Left: offsets from the red sequence for each AGN host are plotted against the AGN's full-band, rest-frame X-ray luminosity. See Section 5.2 for an explanation of the calculation of the RS offsets and Section 5.5 for discussion of X-ray luminosities. The dashed lines separate the galaxies and their AGNs into six regions. Regions 4 and 6 make up the red sequence, Regions 2 and 3 represent the green valley, and Regions 1 and 5 are the blue cloud. Right: EW(Hδ) and $D_n(4000)$ measurements are plotted for the composite spectra for the AGNs in Regions 1–4 of the left-hand panel. Additionally, evolutionary tracks for post-starburst galaxies based on a range of models are displayed. The legend notes the time since last starburst event for galaxies in each region. See Section 4.2 for more details.

cloud. However, the large range of AGN luminosities in the green valley (RS offsets between −3 and −1) is notable. While we found previously in Rumbaugh et al. (2012) that no AGNs inhabited Regions 5 or 6 that correspond to low-luminosity blue AGN hosts and high-luminosity hosts on the red sequence, respectively, we do have a few such objects in our current sample.

We can examine these regions in further detail by looking at their hosts' spectra. As in Sections 4.2 and 5.3, we co-added the spectra to make composite measurements of the hosts' properties. AGNs in each of Regions 1–4 were co-added. The small number of AGNs in Regions 5 and 6 precluded co-addition. To examine the evolutionary states of the AGNs in each region, we measured EW(Hδ) and $D_n(4000)$ for each composite spectrum. The results are plotted in the right-hand panel of Fig. 8. Also plotted are evolutionary tracks for galaxies for varying time since last starburst.

The low values of EW(Hδ) and $D_n(4000)$ indicate that the Region 1 AGNs, which are in the blue cloud, have ongoing or very recent starburst events or concurrent star formation. In contrast, the Region 4 AGNs, which are on the red sequence, have the least recent starburst events, on average. Intermediate to these are the Region 2 and 3 AGNs. Both have had less time than the Region 4 AGNs and more time than the Region 1 AGNs since last starburst, on average. However, the fainter Region 3 AGNs appear to have more recently had starbursts, on average. This conflicts with our previous findings presented in Rumbaugh et al. (2012), which had a smaller sample of 27 AGNs,[10] and where we found that the average Region 2 AGN host had more recently had a starburst event compared to Region 3. The change in the temporal order of the AGNs on the green valley, after increasing sample size, may indicate that green valley AGNs across all luminosities have similar properties or could be a sign of an underlying process that is correlated with X-ray luminosity.

We can conclude though that AGNs across all parts of the CMD have had a starburst, on average, within the last gigayear. There appears to be a close connection between starbursts and AGN activity, particularly for blue cloud and green valley galaxies, especially since the EW(Hδ) values are too large to be attributed to normal star formation. In fact, there seems to be an evolutionary correlation to the host galaxy colours, as blue cloud, green valley and red sequence AGN hosts have had successively more time since the last starburst event, on average.

6 DISCUSSION

We studied AGNs and their host galaxies in 12 LSSs in the ORELSE survey. Using *Chandra* ACIS-I and ACIS-S observations, we identified X-ray point sources in our sample, then matched them to our extensive spectroscopic catalogues using a maximum likelihood technique described in Section 3.4. Our DEIMOS spectroscopic observations have targeted $\gtrsim$1000 objects per field, on average. From this data set, we have obtained redshifts for 288 X-ray point sources, locating 61 AGNs within the LSSs in our sample.

Our sample spans a wide range of environments, from isolated clusters to superclusters, and even includes a system of five merging groups. In addition, our redshift range is from 0.65 to 1.28. These qualities provide an excellent opportunity to study AGN activity and triggering mechanisms. Many of the LSSs in our sample had only a few AGNs, however. Without sufficient numbers to analyse the LSSs alone, we separated our sample into four sub-samples, based on the properties of the LSSs.

To determine how to sub-divide our sample, we measured the average spectral properties of each LSS, as described in Section 4.2. We identified five LSSs that make up what we refer to as the Passive sub-sample. These are mostly isolated clusters at lower redshifts, with lower levels of star formation, well-defined red sequences and low blue fractions. In stark contrast, Cl0849, RXJ0910 and RXJ1053, the highest redshift LSSs in our sample, referred to as the High-z sub-sample, appear to have the most actively star-forming LSS galaxy populations in our sample, both from their average spectral properties and their high fractions of bluer galaxies. In Rumbaugh et al. (2012), we found SG0023 and SC1604 to be the

[10] The sample size of Region 3 AGNs has increased from 10 (7 with $L_x > 10^{42.5}$ erg s^{-1}) to 18.

most active LSSs. While their spectral properties put them at a lower level of average star formation than the High-z sub-sample,[11] and they are not quite as blue, they are still more active than the rest of our sample, so we placed them into their own sub-sample. We are left with SC1324 and RXJ1716 that straddle the line between a quiescent and star-forming average galactic population, in between the Passive sub-sample and SG0023 & SC1604, so we refer to them as the Intermediate sub-sample.

6.1 Analysis of triggering mechanisms

As we explore triggering mechanisms, we first discuss the colours of the AGN host galaxies that provide valuable information on the properties of the host. Some studies have found a correlation between AGN activity and location in the green valley (Sánchez et al. 2004; Nandra et al. 2007; Georgakakis et al. 2008; Silverman et al. 2008; Kocevski et al. 2009; Rumbaugh et al. 2012), although other studies using stellar mass-matched galaxy samples do not find such a correlation (see, e.g. Silverman et al. 2009; Xue et al. 2010). To examine if our AGN hosts cluster in certain regions on a CMD, we analysed their offsets from the red sequence. To compare colours between different LSSs, we calculated RS offsets for each galaxy as described in Section 5.2. We found that AGN hosts were indeed overrepresented in the green valley: 44 per cent of the AGN population was in this region compared to only 27 per cent of the overall population. However, this result is not particularly strong, as a KS test estimated the significance of the difference at less than 90 per cent. When accurate stellar masses are available for our entire sample, we can determine if this association is primarily related to higher mass hosts by comparing to a stellar mass-matched sample.

An association with the green valley on a CMD could provide evidence for a number of different triggering mechanisms. For major mergers, an association would be expected as AGN activity would be coeval with the aftereffects of quenching star formation in blue cloud galaxies. For scenarios involving rejuvenation of red sequence galaxies, AGNs would also tend to lie in the green valley as the host evolves blueward temporarily. Since different mechanisms could be more prominent in different global environmental regimes (e.g. galaxy mergers may be more likely to take place in the outskirts of clusters, where infalling populations lie), we also examined the spatial distributions of our AGN hosts. To compare AGN hosts near the clusters and sub-samples of varying sizes, we employed a phase space metric described in Section 5.1. When separated into four environmental bins based on this metric, as shown in Fig. 4, we found that the phase space distribution of the AGN hosts is very similar to that of the overall galaxy population and a KS test did not provide any significant evidence of difference between them. This result implies that the environment of AGN hosts, whether they are in dense cluster cores, on their outskirts or far from any sub-samples or clusters, has no meaningful effect on their nuclear activity, at least when considering X-ray bright objects. This could mean that major mergers are not the dominant triggering mechanism in our sample, as we would have expected an association with intermediate-density environments, although our results in this regard are only suggestive.

In our analysis of the spectral properties of the AGN hosts in Section 5.3, we found that for all four sub-samples, the average AGN host has more recently had a starburst event compared to the average galaxy in its overall population. This shows a strong correlation between AGN activity and starburst events, across our entire redshift range and LSSs at all levels of star formation activity. This correlation could also be related to the association we found between the green valley and AGN activity: if AGN hosts are more likely to be in the green valley than to be quiescent red sequence galaxies, we may expect them to also have, more recently, a starburst event, on average. However, the difference in time since last starburst for the SG0023 & SC1604 populations exceeded the other sub-samples by a substantial margin. While the overall galaxy populations of these LSSs were not the most actively star-forming, a position held by the High-z sub-sample, the average AGN host in these LSSs, was the most active by far, with the average age since last starburst $\lesssim$100 Myr. The starbursting, or nearly starbursting, AGN hosts in SG0023 & SC1604 appear exceptional and a similar picture is painted by their X-ray luminosity distribution.

Examining the rest-frame X-ray luminosities of the AGNs in our sample, we found some stark contrasts between the different sub-samples. As described in Section 5.5, the Passive-, Intermediate- and High-z sub-samples all had most of their AGNs at lower luminosities, with only two luminosities above $10^{43.5}$ erg s^{-1}, while eight AGNs in SG0023 & SC1604 peak had luminosities above this level. Studies examining cluster AGNs have found that both the AGN fraction and the high-luminosity AGN fraction increase with increasing redshift, up to at least $z \sim 1.5$ (see, e.g. Martini, Sivakoff & Mulchaey 2009; Martini et al. 2013; Alberts et al. 2016). The disproportionately luminous SG0023 & SC1604 AGN population runs counter to this finding, as we do not find a similarly luminous AGN population in the High-z sub-sample. This implies that something different is occurring in SG0023 & SC1604 relative to rest of our sample, which cannot be explained by more star formation activity or a younger overall galaxy population, as the High-z sub-sample has these properties, but does not have a similar luminosity distribution.

Our analysis of the spectral properties and X-ray luminosity distributions of the AGN hosts suggests that some different mechanism is at play in the SG0023 & SC1604 LSSs. One potential explanation could be an increased role of galaxy mergers or tidal interactions in AGN triggering. We examined the possibility by estimating the incidence of galaxy interactions through the proxy of CKPs. While a CKP does not necessarily pick out galaxies undergoing mergers or tidal interactions, a population with higher rates of mergers and tidal interactions should have more galaxies located close to each other, so the CKP fraction should be applicable as a proxy of galaxy interaction rate. We define a CKP as two galaxies within 70 h^{-1} kpc on the sky and 350 km s^{-1} in velocity space. We found that the SG0023 & SC1604 AGN hosts had the highest fraction with CKPs, although we had low precision because of the small number of AGN hosts with CKPs. When looking at the overall galaxy populations, that of SG0023 & SC1604 also had the highest fraction of CKPs. The high CKP fractions are likely indicative of a higher degree of galaxy interactions in these LSSs and could explain the exceptional spectral and X-ray properties of the AGN hosts. This is supported by the morphological analysis of SC1604 carried out by Kocevski et al. (2009), who found that two-thirds of the AGNs examined had signs of recent or pending mergers or tidal interactions.

As a control test, we also examined the properties of field galaxies in our sample. We defined field galaxies as those which, in each observation, were outside the redshift bounds of the LSS observed, but still within the overall redshift range of the sample ($0.65 < z < 1.28$). We found that both the AGN hosts and overall galaxy populations of the field galaxies had low CKP fractions, which is expected given that field galaxies are in less dense environments on

[11] Note that none of the LSSs in the High-z sub-sample were included in Rumbaugh et al. (2012).

average, thus having fewer galaxy interactions. The X-ray luminosity distribution of the field AGNs at $z < 0.96$ peaked in the lowest energy bin, similarly to the Passive-, Intermediate- and High-z sub-samples. The field AGNs at $z > 0.96$ (the redshift of the High-z sub-sample) peaked at a slightly higher energy, but still at lower energies than for SG0023 & SC1604. The higher luminosities of the higher redshift field AGNs could be explained by larger available gas reservoirs to fuel AGNs in the bluer galaxies at these redshifts. These results imply that similar processes are triggering AGNs in the field galaxies and in the Passive-, Intermediate- and High-z sub-samples, while some different mechanism is substantially more prominent for those in SG0023 & SC1604. The CKP fractions and the expected low merger rate in the field populations provide evidence that the galaxies in SG0023 & SC1604 have more mergers or tidal interactions occurring, which are triggering AGN activity.

The X-ray luminosities of the AGNs in our sample, in conjunction with the RS offsets, provide further information on triggering and evolutionary processes. When these properties are plotted against each other, as in Fig. 8, a correlation can be seen. Those in the blue cloud tend to be more X-ray luminous, while those on the red sequence are overwhelmingly less luminous. There is a wide range of X-ray luminosities for AGNs hosted by the green valley galaxies. The difference between the AGNs in blue and red hosts could be explained by larger gas reservoirs available in bluer galaxies. If the green valley is a transition region where blue cloud galaxies are rapidly evolving on to the red sequence and this transition is related to AGN activity, we would expect these colour–luminosity trends as well. AGNs triggered in blue cloud galaxies would start out at the most luminous end of the distribution. As star formation is quenched, the galaxy's colour evolves towards red, at the same time as a drop in AGN luminosity as it loses its fuel source.

In the left-hand panel of Fig. 8, we have demarcated Regions 1–4 that correspond to blue galaxies with bright AGNs, green galaxies with bright AGNs, green galaxies with faint AGNs and red sequence galaxies with faint AGNs, respectively. If we constructed composite spectra of the AGNs in each region, we might expect the EW(Hδ) and $D_n(4000)$ measurements to paint a picture where AGN hosts have had more time since the last starburst event as you look sequentially at Regions 1–3 and then 4. This is what we found in Rumbaugh et al. (2012), where our sample consisted of just 27 AGNs in SG0023, SC1324, SC1604, RXJ1757 and RXJ1821, compared to 61 now. When we perform this same exercise with our current sample, we find again that the average Region 1 AGNs and the Region 4 AGNs have most and least recently had starburst events, respectively, but the situation has been reversed for those on the green valley. As shown in Fig. 8, Region 3 AGNs, on average, appear to more recently have starburst events, on average, compared to the more X-ray luminous Region 2 AGNs. This cannot be explained due to the uncertainties on the measurements. This implies that something more complicated is occurring than a simple scenario wherein all AGNs and their hosts begin in Region 1 with their triggering and evolve into Region 4 over time.

Of note, SG0023 & SC1604 are overrepresented in Region 1. After our analysis in Rumbaugh et al. (2012), we expected to add more objects to this region as our sample size increased.[12] However, despite the number of AGNs in our sample rising from 27 to 61, we added only one X-ray luminous, blue cloud AGN. Similarly, we added only two X-ray luminous, green valley AGNs. We disproportionately added AGNs in Regions 3 and 4, leaving Regions 1 and 2 dominated by SG0023 & SC1604. This trend seems to indicate that SG0023 & SC1604 are exceptional when compared to the general sample. We have already established that these LSSs seem to have an elevated level of galaxy interactions, which likely affects the AGN activity within them. Our new results could be explained if two AGN evolutionary scenarios were occurring. First, merger-induced AGNs would tend to trigger in Region 1 and would evolve sequentially through Regions 2 and 3 and end up in Region 4. A second process would tend to create less luminous AGNs that would be triggered in Region 3 and evolve into Region 4. While there is still a population of merger-induced AGNs that fit on the track moving through Regions 1–4, the second class of AGNs would lead to a decrease in the average time since last starburst in Region 3, explaining this new result.

The exact nature of this second triggering mechanism is not something our data can fully illuminate. A number of possible mechanisms for AGN activation have been proposed as alternatives to major galaxy mergers, such as minor mergers or tidal interactions (Menanteau et al. 2001), disc or bar instabilities or recycling of stellar material (Ciotti & Ostriker 2007), and some studies have proposed gradual ramp-downs of accretion and luminosity to explain low-luminosity AGNs (Croton et al. 2006; McNamara & Nulsen 2007; Shen et al. 2007). If minor mergers were the second prominent trigger, we would expect to see increased activity for this AGN mode in the LSSs with high CKP fractions, as increased galaxy interactions should create both more major and minor mergers. As such, our data do not prefer this possibility, since the second mechanism is not exclusive to SG0023 & SC1604. Moving beyond minor mergers, a detailed morphological study needs to be performed, requiring high-resolution, multiband data across the entire sample, to search for galaxies with signs of recent mergers or interactions to definitively rule on the issue, and further substantiate our results here, as well as to search for blue galaxy cores that would be signatures of some of these mechanisms. Alternatively, precise measurements of the local density for every AGN host, and galaxy in the overall population, could shed more light on where galaxy mergers and interactions are most likely to occur and we plan to use this method to study the ORELSE sample, as in Lemaux et al. (in prep.). Using this method, we will look for specific differences between the AGN hosts and the underlying galaxy populations in SG0023 & SC1604, as well as relative to the rest of the LSSs.

6.2 Comparisons to previous work

Other AGN studies have found results both similar and differing from ours, although this may be unsurprising given the conflicting evidence on AGN triggering mechanisms. Alberts et al. (2016), for example, studied AGNs in ∼250 galaxy clusters at $0.5 < z < 2$ from the IRAC Shallow Cluster Survey and the IRAC Distant Cluster Survey. They found an excess AGN fraction at $z > 1$ compared to lower redshifts, with the fraction exceeding the field at $z > 1.5$. They argue that this is evidence for the increasing prevalence of merger-induced AGN activity at higher redshifts, but this is not reflected in our data set. It is possible this is due to small number statistics, since we only studied three LSSs at higher redshifts than SG0023 & SC1604. With a larger $z > 1$ sample, we may also find more LSSs like SG0023 & SC1604. Ehlert et al. (2015) also find evidence for merger-induced AGN activity, analysing >11000 *Chandra*-selected AGNs in and behind 135 massive ($\gtrsim 10^{14}$ $M_\odot$) galaxy clusters at $0.2 < z < 0.9$. They find a spatial dependence on AGN fraction, with an excess in the central regions of clusters, a result not reflected in our data. Additionally, AGN abundance in their data set scales

[12] Note that all new observations in this study were from outside SG0023 & SC1604.

with the parent cluster mass as $M_{500}^{-1.2}$, showing a suppression at higher masses. This is similar to the galaxy merger rate, suggesting a connection, compounded by a higher incidence of disturbed morphologies among AGN hosts. Rosario et al. (2015) used Cosmic Assembly Near Infrared Extragalactic Legacy Survey (CANDELS) *HST* imaging and far-IR imaging from the PEP+GOODS-*Herschel* survey to study >100 X-ray-selected AGNs in two *Chandra* deep fields. Similarly to the previous studies, they find a higher incidence of clumpy morphologies suggestive of recent mergers among AGN hosts compared to inactive galaxies at $z \sim 1$, although the connection weakens towards $z \sim 2$.

Providing evidence against mergers as AGN triggers, Koulouridis et al. (2014) find no suppression of AGN activity at high densities relative to the field, examining X-ray-selected AGNs in 33 galaxy clusters in the *XMM–Newton* LSS sample at $0.14 < z < 1.05$. They do use a lower mass sample of galaxy clusters than Ehlert et al. (2015), which includes only $\gtrsim 10^{14}$ M$_\odot$ clusters. The lack of correlation between our phase space metric, $p = r_{\rm norm} \times v_{\rm norm}$, and AGN fraction could similarly result from the lower masses of galaxy clusters and groups relative to Ehlert et al. (2015). Additionally, Hernández-Ibarra et al. (2016) analysed SDSS-DR7 spectra of 385 isolated pairs of galaxies ($\Delta v \leq 1200$ km s^{-1}, $r \leq 100$ kpc). When compared to the 513 isolated galaxies studied by Hernández-Ibarra et al. (2013), they find similar AGN fractions, albeit at low luminosities ($L_{\rm H\,\alpha} \sim 2 \times 10^{40}$ erg s^{-1}). This result does leave open the possibility that major mergers trigger high-luminosity AGNs and is consistent with our findings that low-luminosity AGNs are not triggered by minor mergers or interactions. Kocevski et al. (2012) examine *HST*/Wide Field Camera imaging from CANDELS of 72 moderate luminosity ($L_X \sim 10^{42–44}$ erg s^{-1}) AGN hosts at $1.5 < z < 2$, selected using the 4 Ms *Chandra* Deep Field South. Similarly, they find that both AGN hosts and non-active galaxies have similar fractions with disturbed morphologies, which is consistent with the $z \sim 2$ sub-sample of Rosario et al. (2015). This may continue the trend observed in our sample, where our $z > 1$ LSSs had CKP fractions and X-ray luminosity distributions similar to the field, but does not preclude major mergers playing an important role at lower redshift.

One of the most unique aspects of our sample relative to other studies is the approximately binary nature of the possibly merger-induced, high-luminosity AGNs. Rather than merely correlating with an environmental or host property such as CKP fraction, these high-luminosity AGNs are concentrated almost entirely within two LSSs. This suggests the merger AGN mode is almost entirely suppressed elsewhere. While our results may be influenced by a small sample size, in that only two LSSs appeared to show a preference for merger-induced AGN activity, they may suggest that the properties of some LSSs make them especially prone to trigger AGNs through major galaxy mergers, although with only two such LSSs, we are unable to determine their exact nature.

While previous work has found mixed evidence for merger-induced AGN activity, this could be explained by multiple triggering scenarios. The differing results could be the result of differing sample selections, leading to many different cross-sections of the merger-induced AGN population. The data from the SG0023 & SC1604 LSSs do provide evidence that galaxy mergers are important for triggering AGNs in some regimes, while the rest of our sample, and the similarities to our field AGNs, shows that at least one other mechanism plays a significant role.

7 SUMMARY

We studied AGNs and their hosts in 12 LSSs, using *Chandra* observations, optical and NIR imaging and spectroscopy, seeking to explore triggering mechanisms. We found a total of 61 AGNs, matched to spectroscopically confirmed hosts, within the LSSs in our sample. The hosts were associated with starbursts; the spectral features of their composite spectra indicated that the AGN populations more recently had starburst events than their parent populations, on average. The hosts were also found to be associated with the green valley on a CMD, but did not seem to be associated with any particular environment within the LSSs. These results do not particularly favour any triggering mechanism.

Two LSSs in our sample, SG0023 and SC1604, had a number of exceptional properties relative to the others. Their populations had disproportionately more X-ray luminous AGNs, they had the most recent starburst events, on average, and both the AGN hosts and the overall galaxy populations had significantly higher CKP fractions. The last point indicates that galaxy mergers and interactions are happening more frequently in these LSSs compared to the others. The evidence suggests that the AGNs in SG0023 and SC1604 are being triggered by galaxy mergers. For the rest of the LSSs, other mechanisms should be dominant. This can be checked by looking at the field AGNs in our sample, which should have relatively low merger rates. Indeed, the field populations have low CKP fractions and their X-ray luminosity distributions looked more like the other LSSs than like SG0023 and SC1604. The combination of these results suggests that major mergers are the dominant triggers of AGNs in some regimes, such as those represented by SG0023 and SC1604, while other mechanisms dominate elsewhere and produce a population of lower luminosity AGNs. While there are many possibilities for other mechanisms, minor mergers are unlikely, as the same conditions that produce major mergers in SG0023 and SC1604 more frequently should produce minor ones as well.

ACKNOWLEDGEMENTS

This material is based upon work supported by the National Aeronautics and Space Administration under NASA Grant Number NNX15AK92G. The authors thank Kirpal Nandra and Antonis Georgakakis for providing the Imperial reduction pipeline and their ongoing support of the software. The spectroscopic data presented herein were obtained at the W.M. Keck Observatory, which is operated as a scientific partnership among the California Institute of Technology, the University of California and the National Aeronautics and Space Administration. The Observatory was made possible by the generous financial support of the W.M. Keck Foundation. The authors wish to recognize and acknowledge the very significant cultural role and reverence that the summit of Mauna Kea has always had within the indigenous Hawaiian community. We are most fortunate to have the opportunity to conduct observations from this mountain.

REFERENCES

Alberts S. et al., 2016, ApJ, 825, 72
Ascaso B., Lemaux B. C., Lubin L. M., Gal R. R., Kocevski D. D., Rumbaugh N., Squires G., 2014, MNRAS, 442, 589
Barrera-Ballesteros J. K. et al., 2015, A&A, 582, A21
Bluck A. F. L., Conselice C. J., Almaini O., Laird E. S., Nandra K., Grützbauch R., 2011, MNRAS, 410, 1174
Bournaud F. et al., 2011, ApJ, 730, 4
Boyle B. J., Terlevich R. J., 1998, MNRAS, 293, L49
Brammer G. B., van Dokkum P. G., Coppi P., 2008, ApJ, 686, 1503
Bruzual G., 2007, in Vallenari A., Tantalo R., Portinari L., Moretti A., eds, ASP Conf. Ser. Vol. 374, From Stars to Galaxies: Building the Pieces to Build Up the Universe. Astron. Soc. Pac., San Francisco, p. 303

Bruzual G., Charlot S., 2003, MNRAS, 344, 1000
Ciotti L., Ostriker J. P., 2007, ApJ, 665, 1038
Cisternas M. et al., 2011, ApJ, 741, L11
Contini T. et al., 2016, A&A, 591, A49
Croton D. J. et al., 2006, MNRAS, 365, 11
Dressler A., Smail I., Poggianti B. M., Butcher H., Couch W. J., Ellis R. S., Oemler A., Jr1999, ApJS, 122, 51
Dressler A., Oemler A., Jr, Poggianti B. M., Smail I., Trager S., Shectman S. A., Couch W. J., Ellis R. S., 2004, ApJ, 617, 867
Dressler A., Oemler A., Jr, Poggianti B. M., Gladders M. D., Abramson L., Vulcani B., 2013, ApJ, 770, 62
Ehlert S. et al., 2015, MNRAS, 446, 2709
Ellison S. L., Mendel J. T., Scudder J. M., Patton D. R., Palmer M. J. D., 2013, MNRAS, 430, 3128
Elmegreen B. G. et al., 1998, ApJ, 503, L119
Ettori S., Tozzi P., Borgani S., Rosati P., 2004, A&A, 417, 13
Faber S. M. et al., 2003, in Iye M., Moorwood A. F. M., eds, Proc. SPIE Conf. Ser. Vol. 4841, Instrument Design and Performance for Optical/Infrared Ground-based Telescopes. SPIE, Bellingham, p. 1657
Faber S. M. et al., 2007, ApJ, 665, 265
Fazio G. G. et al., 2004, ApJS, 154, 10
Ferrarese L., Merritt D., 2000, ApJ, 539, L9
Fioc M., Rocca-Volmerange B., 1997, A&A, 326, 950
Ford H. C., Tsvetanov Z. I., Ferrarese L., Jaffe W., 1998, in Sofue Y., ed., Proc. IAU Symp. 184, The Central Regions of the Galaxy and Galaxies. Kluwer, Dordrecht, p. 377
Fruscione A. et al., 2006, in Silva D. R., Doxsey R. E., eds, Proc. SPIE Conf. Ser. Vol. 6270, Observatory Operations: Strategies, Processes, and Systems. SPIE, Bellingham, p. 1
Gal R. R., Lubin L. M., 2004, ApJ, 607, L1
Gal R. R., Lemaux B. C., Lubin L. M., Kocevski D., Squires G. K., 2008, ApJ, 684, 933
Gehrels N., 1986, ApJ, 303, 336
Genzel R. et al., 2008, ApJ, 687, 59
Georgakakis A. et al., 2008, MNRAS, 385, 2049
Georgakakis A. et al., 2009, MNRAS, 397, 623
Georgantopoulos I., Rovilos E., Comastri A., 2011, A&A, 526, A46
Gill S. P. D., Knebe A., Gibson B. K., 2005, MNRAS, 356, 1327
Gilmour R., Gray M. E., Almaini O., Best P., Wolf C., Meisenheimer K., Papovich C., Bell E., 2007, MNRAS, 380, 1467
Gioia I. M., Wolter A., Mullis C. R., Henry J. P., Böhringer H., Briel U. G., 2004, A&A, 428, 867
Gladders M. D., Yee H. K. C., 2005, ApJS, 157, 1
Gladders M. D., López-Cruz O., Yee H. K. C., Kodama T., 1998, ApJ, 501, 571
Gladders M. D., Yee H. K. C., Ellingson E., 2002, AJ, 123, 1
Graham A. W., 2016, Astrophysics and Space Science Library, Vol. 418, Galactic Bulges. Springer International Publishing, Switzerland, p. 263
Haines C. P. et al., 2012, ApJ, 754, 97
Häring N., Rix H.-W., 2004, ApJ, 604, L89
Hashimoto Y., Hasinger G., Arnaud M., Rosati P., Miyaji T., 2002, A&A, 381, 841
Hashimoto Y., Henry J. P., Hasinger G., Szokoly G., Schmidt M., 2005, A&A, 439, 29
Hasinger G. et al., 1998, A&A, 340, L27
Heckman T. M., Best P. N., 2014, ARA&A, 52, 589
Heckman T. M., Kauffmann G., Brinchmann J., Charlot S., Tremonti C., White S. D. M., 2004, ApJ, 613, 109
Henry J. P. et al., 1997, AJ, 114, 1293
Hernández-Ibarra F. J., Dultzin D., Krongold Y., Olmo A. d., Perea J., González J., 2013, MNRAS, 434, 336
Hernández-Ibarra F. J., Krongold Y., Dultzin D., del Olmo A., Perea J., González J., Mendoza-Castrejón S., Bitsakis T., 2016, MNRAS, 459, 291
Hewett P. C., Warren S. J., Leggett S. K., Hodgkin S. T., 2006, MNRAS, 367, 454
Hicks A. K. et al., 2007, ApJ, 671, 1446
Hicks A. K. et al., 2008, ApJ, 680, 1022
Holden B. P., Stanford S. A., Squires G. K., Rosati P., Tozzi P., Eisenhardt P., Spinrad H., 2002, AJ, 124, 33
Hopkins P. F., Quataert E., 2010, MNRAS, 407, 1529
Hopkins P. F., Hernquist L., Cox T. J., Di Matteo T., Robertson B., Springel V., 2006, ApJS, 163, 1
Jeltema T. E., Canizares C. R., Bautz M. W., Buote D. A., 2005, ApJ, 624, 606
Juneau S. et al., 2013, ApJ, 764, 176
Kauffmann G. et al., 2003, MNRAS, 346, 1055
Kim M. et al., 2007, ApJS, 169, 401
Kocevski D. D., Lubin L. M., Lemaux B. C., Gal R. R., Fassnacht C. D., Lin R., Squires G. K., 2009, ApJ, 700, 901
Kocevski D. D. et al., 2012, ApJ, 744, 148
Kormendy J., Ho L. C., 2013, ARA&A, 51, 511
Kormendy J., Richstone D., 1995, ARA&A, 33, 581
Koss M., Mushotzky R., Veilleux S., Winter L., 2010, ApJ, 716, L125
Koulouridis E. et al., 2014, A&A, 567, A83
Kriek M., van Dokkum P. G., Labbé I., Franx M., Illingworth G. D., Marchesini D., Quadri R. F., 2009, ApJ, 700, 221
Laird E. S. et al., 2009, ApJS, 180, 102
Laird E. S., Nandra K., Pope A., Scott D., 2010, MNRAS, 401, 2763
Lemaux B. C. et al., 2009, ApJ, 700, 20
Lemaux B. C., Lubin L. M., Shapley A., Kocevski D., Gal R. R., Squires G. K., 2010, ApJ, 716, 970
Lemaux B. C. et al., 2012, ApJ, 745, 106
Lemaux B. C. et al., 2014, A&A, 572, A90
Lubin L. M., Gal R. R., Lemaux B. C., Kocevski D. D., Squires G. K., 2009, AJ, 137, 4867
Mamon G. A., Sanchis T., Salvador-Solé E., Solanes J. M., 2004, A&A, 414, 445
Marconi A., Hunt L. K., 2003, ApJ, 589, L21
Martini P., Sivakoff G. R., Mulchaey J. S., 2009, ApJ, 701, 66
Martini P. et al., 2013, ApJ, 768, 1
McNamara B. R., Nulsen P. E. J., 2007, ARA&A, 45, 117
Menanteau F., Jimenez R., Matteucci F., 2001, ApJ, 562, L23
Miyazaki S. et al., 2002, PASJ, 54, 833
Moore B., Katz N., Lake G., Dressler A., Oemler A., 1996, Nature, 379, 613
Mullis C. R. et al., 2003, ApJ, 594, 154
Nandra K. et al., 2007, ApJ, 660, L11
Nandra K. et al., 2015, ApJS, 220, 10
Narayanan D. et al., 2008, ApJS, 176, 331
Nazaryan T. A., Petrosian A. R., Hakobyan A. A., McLean B. J., Kunth D., 2014, Astrophysics, 57, 14
Netzer H., 2015, ARA&A, 53, 365
Newman J. A. et al., 2013, ApJS, 208, 5
Noble A. G., Webb T. M. A., Muzzin A., Wilson G., Yee H. K. C., van der Burg R. F. J., 2013, ApJ, 768, 118
Oke J. B., Postman M., Lubin L. M., 1998, AJ, 116, 549
Poggianti B. M., Barbaro G., 1997, A&A, 325, 1025
Oemler, Jr, A.Poggianti B. M., Smail I., Dressler A., Couch W. J., Barger A. J., Butcher H., Ellis R. S.1999, ApJ, 518, 576
Puget P. et al., 2004, in Moorwood A. F. M., Iye M., eds, Proc. SPIEConf. Ser. Vol. 5492, Ground-based Instrumentation for Astronomy. SPIE, Bellingham, p. 978
Ranalli P., Comastri A., Setti G., 2003, A&A, 399, 39
Reichard T. A., Heckman T. M., Rudnick G., Brinchmann J., Kauffmann G., Wild V., 2009, ApJ, 691, 1005
Robotham A. S. G. et al., 2014, MNRAS, 444, 3986
Rosario D. J. et al., 2012, A&A, 545, A45
Rosario D. J. et al., 2015, A&A, 573, A85
Rosati P., Della Ceca R., Norman C., Giacconi R., 1998, ApJ, 492, L21
Rosati P., Stanford S. A., Eisenhardt P. R., Elston R., Spinrad H., Stern D., Dey A., 1999, AJ, 118, 76
Rumbaugh N., Kocevski D. D., Gal R. R., Lemaux B. C., Lubin L. M., Fassnacht C. D., McGrath E. J., Squires G. K., 2012, ApJ, 746, 155
Rumbaugh N., Kocevski D. D., Gal R. R., Lemaux B. C., Lubin L. M., Fassnacht C. D., Squires G. K., 2013, ApJ, 763, 124
Sánchez S. F. et al., 2004, ApJ, 614, 586

Schawinski K., Treister E., Urry C. M., Cardamone C. N., Simmons B., Yi S. K., 2011, ApJ, 727, L31
Schawinski K., Simmons B. D., Urry C. M., Treister E., Glikman E., 2012, MNRAS, 425, L61
Shen Y., Mulchaey J. S., Raychaudhury S., Rasmussen J., Ponman T. J., 2007, ApJ, 654, L115
Silverman J. D. et al., 2008, ApJ, 675, 1025
Silverman J. D. et al., 2009, ApJ, 696, 396
Simcoe R. A., Metzger M. R., Small T. A., Araya G., 2000, BAAS, 32, 758
Stanford S. A., Elston R., Eisenhardt P. R., Spinrad H., Stern D., Dey A., 1997, AJ, 114, 2232
Stanford S. A., Holden B., Rosati P., Tozzi P., Borgani S., Eisenhardt P. R., Spinrad H., 2001, ApJ, 552, 504
Stott J. P., Pimbblet K. A., Edge A. C., Smith G. P., Wardlow J. L., 2009, MNRAS, 394, 2098
Sutherland W., Saunders W., 1992, MNRAS, 259, 413
Tanaka M. et al., 2008, A&A, 489, 571
Taylor E. L. et al., 2005, MNRAS, 361, 1352
Treister E., Schawinski K., Urry C. M., Simmons B. D., 2012, ApJ, 758, L39
Tremaine S. et al., 2002, ApJ, 574, 740
Veilleux S. et al., 2009, ApJS, 182, 628
Vikhlinin A., McNamara B. R., Forman W., Jones C., Quintana H., Hornstrup A., 1998, ApJ, 502, 558
Vikhlinin A., van Speybroeck L., Markevitch M., Forman W. R., Grego L., 2002, ApJ, 578, L107
Vikhlinin A. et al., 2009, ApJ, 692, 1033
Voges W. et al., 1996, in Zimmermann H. U., Trümper J., Yorke H., eds, Roentgenstrahlung from the Universe. p. 637
Wild V., Kauffmann G., Heckman T., Charlot S., Lemson G., Brinchmann J., Reichard T., Pasquali A., 2007, MNRAS, 381, 543
Wise M. W., Davis J. E., Heunnemoerder S., Houck J. C., Dewey D., 2003, MARX 4.0 Technical Manual. MIT Center for Space Research, Cambridge, MA
Wisnioski E. et al., 2015, ApJ, 799, 209
Xue Y. Q. et al., 2010, ApJ, 720, 368
Xu B.-X., Wu X.-B., Zhao H.-S., 2007, ApJ, 664, 198
Yan R., Newman J. A., Faber S. M., Konidaris N., Koo D., Davis M., 2006, ApJ, 648, 281
Younger J. D., Hopkins P. F., Cox T. J., Hernquist L., 2008, ApJ, 686, 815

APPENDIX A: COMPLETENESS AND SELECTION EFFECTS

A1 X-ray completeness

Estimating the limiting luminosities of our *Chandra* observations is not straightforward. One of the main reasons for this is that for each object, we had three chances to detect it, once in each of the three energy bands we considered: the soft (0.5–2.0 keV), hard (2.0–7.0 keV) and full (0.5–7.0 keV) bands. Note that the energy range of the full band is simply the sum of the soft and hard bands, which adds the complication that the three bands are not independently observed. Furthermore, the relatively small number of counts per source brings us into the regime where Poisson statistics are highly relevant. So, to estimate the completeness of our X-ray detections, we carried out an MC simulation to take these effects, and others, into account.

There are a number of variables that influence X-ray point source detection. Some are dependent on the field or observation, including the energy band of the observation, the background emission level and the exposure time. Others vary between sources or across the field of view, such the intrinsic luminosity of the sources, their redshifts and their off-axis angle. The latter refers to the distance on the detector from the *Chandra* aimpoint, and the PSF is highly dependent upon it, as well as on the energy, varying from subarcsecond near the aimpoint to tens of arcseconds at the edges of the ACIS-I array (off-axis angles $\gtrsim 10$ arcsec). Because of this, the X-ray completeness will vary substantially across the field of view. This makes describing the X-ray completeness difficult. If the entire field of view is considered for each LSS, the completeness will be quite low. However, we are not interested so much in finding every AGN in the field of view as comparing numerical measurements within our sample. As such, it is sufficient to examine a similar area within each observation and compare completeness within those areas. We choose for this area a circle with radius 3 arcmin centred on the *Chandra* aimpoint.

For each LSS, we consider the completeness at specific redshifts, in the range $0.65 < z < 1.25$, with steps of $\Delta z = 0.05$. For each redshift, we generated 100 000 sources within the 3 arcmin centred on the *Chandra* aimpoint for that observation. Each source was assigned a rest-frame, full-band X-ray luminosity drawn from a uniform distribution, in log-space, in the range 10^{42}–$10^{44.5}$ erg s^{-1}. To determine the luminosities in the soft and hard bands, each source was also assigned a hardness ratio, drawn from the smoothed distribution of hardness ratios we observed in our sample.

After all points were generated, the observed fluxes were calculated using a power-law spectral model with $\Gamma = 1.4$. The next step is to convert these fluxes into expected photon counts observed. The factor for this conversion varies from source to source when calculated using the Imperial Pipeline discussed briefly in Section 3.3 and in more detail in Laird et al. (2009) and Nandra et al. (2015). However, it is approximately constant across each pointing. So, for each pointing in the soft and hard bands, we performed a linear fit to the relation between the net counts observed for each source and the flux calculated for that source. Using this value for all generated sources, we then estimated the expected photon counts in each band for each source. For each source, counts were 'measured' within an aperture defined by the PSF at that position, designed to enclose 95 per cent of the flux for the soft band and 90 per cent in the hard band. The 'measured' counts are the sum of the source counts and background counts, so the background counts also had to be simulated. To estimate the background levels, the images for each LSS were binned to 64 pixels (at 0.492 arcsec per *Chandra* pixel). For each source, the background level of the closest bin was used. The counts for each source were then drawn from a Poisson distribution defined by the total number of expected counts (source plus background) in the aperture. Background counts for each source were also generated for a background annulus, with inner radius and outer radius 1.5 and 2.5 times the aperture radii, respectively. These were drawn from a Poisson distribution defined by the expected number of background counts in the annulus. The net counts in the soft and hard counts could then be calculated by subtracting the total counts generated in the apertures by the scaled background counts generated in the annuli, which mimics our observations. The full-band net counts were then just the sum of the soft and hard band net counts.[13]

Each source could then be assigned a detection significance, using the formula $\sigma = C/\left(1+\sqrt{0.75+B}\right)$, where C are the net photon counts and B are the background counts in the aperture. As in our analysis, we define as detected all sources with $\sigma > 2$ in at least one band. We then bin all sources for each pointing and each redshift step into intrinsic rest-frame luminosity bins and calculate

[13] While the full-band net counts will not necessarily equal the sum of those in the soft and hard bands for our actual data reduction, our method in this section is simplified, as was necessary to make the simulation feasible.

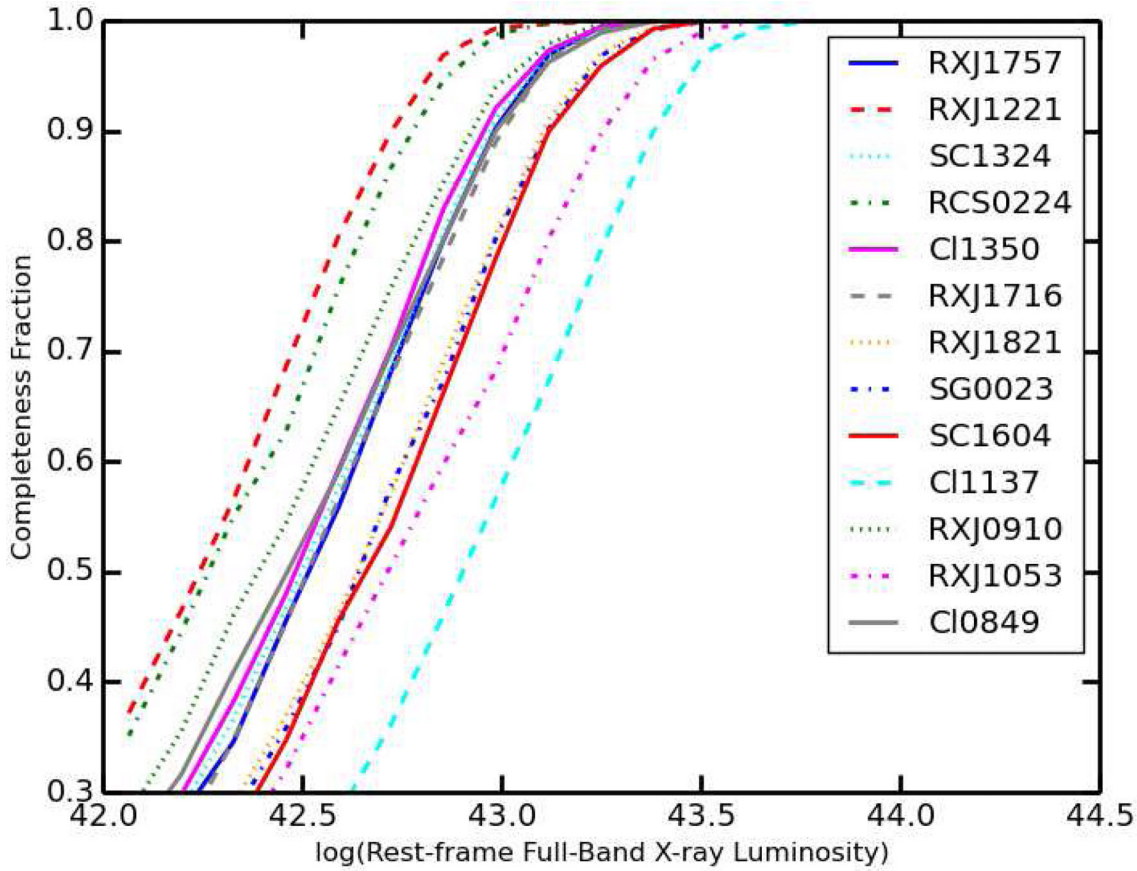

Figure A1. Results of X-ray completeness MC simulations are shown for each LSS as a function of rest-frame, full-band X-ray luminosity, at the redshift closest to $\langle z \rangle$ for that LSS. Completeness is measured here as the fraction of sources detected in a given luminosity bin in our simulation divided by the total number of simulated sources with that intrinsic luminosity. While Cl1137 is not included in our analysis, it is included in this figure for comparison.

Table A1. Results of X-ray completeness MC simulation.

LSS sub-sample or field population	Per cent complete luminosity range (log)				
	42–42.5	42.5–43	43–43.5	43.5–44	44.5–44.5
Passive	38.9	78.7	98.7	100	100
Intermediate	32.8	74.0	98.7	100	100
SG0023 & SC1604	24.4	61.6	95.1	100	100
High-z	33.8	70.0	95.4	100	100
Field (all)	30.8	65.6	92.7	99.7	100
Field ($z < 0.8$)	45.4	84.2	99.5	100	100
Field ($0.8 < z < 0.96$)	32.4	70.0	96.5	100	100
Field ($z > 0.96$)	22.4	53.3	86.8	99.4	100

the completeness within each bin, defined here as the number of sources detected in that luminosity bin divided by the total number of sources in that luminosity bin.

The full-band completeness (hereafter, luminosities mentioned are full-band) is plotted for each LSS in Fig. A1, at the redshift step closest to $\langle z \rangle$ (see Table 1) in each case. Note that Cl1137 is included in this plot, but not in the analysis in any other part of the paper. The reason for this is summarized in this figure, where the completeness for Cl1137 in 10–15 per cent lower than any other field across the luminosity range $10^{42.5}$–10^{43} erg s^{-1}. For all other fields, we can see completeness is almost unity above 10^{43} erg s^{-1}. Completeness begins falling off below this value and is at 35–70 per cent at $10^{42.5}$ erg s^{-1}. The completeness fractions are more succinctly summarized in Table A1, where the fractions are averaged over the five luminosity bins between 10^{42} and $10^{44.5}$ erg s^{-1} in log-space. In addition to the completeness fractions for each field, the average completeness fractions for each of the four sub-samples described in Section 4.3 are shown, as well as the combined completeness fractions for the field populations[14] across all observations.[15] We

[14] Field galaxies are defined as those within the redshift range of the ORELSE sample ($0.65 < z < 1.28$), but outside the redshift bounds of the LSS in their *Chandra* observation.

[15] In these averages, the LSSs with two pointings, SC1324 and SC1604, are accorded double weighting. Additionally, Cl1137 is not included for these average measurements.

can see that the average completeness approximately ranges from 55 per cent to 90 per cent in the luminosity range $10^{42.5}$–10^{43} erg s^{-1}, but falls to approximately 25 per cent to 50 per cent below this for the LSSs. For this reason, we cut objects with luminosities below $10^{42.5}$ erg s^{-1}. While the average completeness of each sub-sample is within 20 per cent, the histogram in Fig. 7 can be corrected to account for the individual completeness values. However, our results are not significantly affected by this correction.

When considering the field galaxies, there is a wider range of completeness estimates for the $10^{42.5}$–10^{43} erg s^{-1} luminosity bin, ranging from 53 per cent for highest redshift galaxies to 84 per cent for the lowest galaxies. Correcting the field galaxy luminosity distribution in Fig. 7 accounts for some of the discrepancy between the different luminosity distributions of the three field galaxy redshift bins.

A2 Spectroscopic completeness

While some of our LSSs, such as SC1604, have nearly complete spectroscopy to $m_{\rm I} \leq 24$, or $M_{\rm red} \leq -20.9$, this is not the case in general. Therefore, it is possible that some AGN hosts have been missed by our spectroscopic coverage so far. Since our initial spectral masks tended to target redder galaxies deemed more likely to be LSS members, varying levels of spectroscopic completeness could create biases between the observed AGN populations of the different LSSs.

To determine the effects of incomplete spectroscopy, we used our photometric catalogues, described in Section 3.1. For a subset of our sample, we used our photometry to estimate photometric redshifts, as discussed in Section 3.1.1 and in more detail in Tomczak et al. (2016, in preparation). In this process, we derived $P(z)$ for each source, which estimates the probability that any given redshift is the true redshift for that source. When $P(z)$ is integrated over a redshift range, it should give the probability that the source actually lies in that given range. So, we can use $P(z)$ to estimate the probability that sources without spectroscopic redshifts are members of a given LSS, by integrating over the redshift bounds of that LSS. With this method, we calculate the expected number of new AGNs that would be added as LSS members if we were to complete our spectroscopy, for the fields where photometric redshifts have been calculated. This is accomplished by calculating

$$\sum_i \int_{z_{\rm LB}}^{z_{\rm UB}} P_i\,(z)\,{\rm d}z, \tag{A1}$$

where $z_{\rm LB}$ and $z_{\rm UB}$ are the redshift bounds of that LSS. The sum is over all sources without high-quality spectroscopic redshifts, including only objects within our spectral coverage on the sky.

This method relies on the sample being tested to have an approximately uniform true distribution in redshift space, at least in the area where $P(z)$ has a non-negligible overlap with the redshift range being considered. This can be seen by examining equation (A1). Each term in the sum corresponds to one source and adds between 0 and 1 to the total, which is the total number of expected new sources. Therefore, the sum must be less than or equal to the total number of sources being considered. This means that if all these sources are true LSS members, equation (A1) necessarily underestimates the expected number of sources. The degree of underestimation is determined by the shape of the average $P(z)$ relative to the width of the LSS in redshift space. If the average $P(z)$ has substantial values outside of the redshift range, the estimated number of new sources will be considerably lower than the actual number. If the sample being considered includes sources actually located outside the LSS, those sources add to the sum in equation (A1), which can compensate for the underestimation of the number of actual LSS members. As the true redshift distribution of the sample approaches uniformity, these outside sources bring the estimated number of sources in the LSS towards matching the true number, assuming $P(z)$ is similar in shape throughout the sample, on average. While we do not know the true redshift distribution of the sources being tested, this method should give us reasonable estimates of the number of sources we expect to add through completing spectroscopy.

When we apply this technique to the LSSs with photometric redshift catalogues, and ignoring objects where equation (A1) gives a probability of measurements less than 5 per cent, we estimate that 0.2, 1.7, 0, 0, 0.8, 0 and 0.2 X-ray point sources would be added as LSS members for SG0023, RXJ0910, SC1324, SC1604, RXJ1716, RXJ1757 and RXJ1821, respectively, with complete spectroscopy. On average, over these LSSs, this is an increase in sample size of only $\sim$10 per cent, so our results should not be significantly affected by spectroscopic incompleteness.

This paper has been typeset from a TEX/LATEX file prepared by the author.